---

**Article:**
Middleton, T.A., Walker, R.T., Rood, D.H. et al. (2016) The tectonics of the western Ordos Plateau, Ningxia, China: Slip rates on the Luoshan and East Helanshan Faults. Tectonics, 35 (11). pp. 2754-2777. ISSN: 0278-7407

https://doi.org/10.1002/2016TC004230

---

This is the peer reviewed version of the following article: Middleton, T. A. et al (2016), The tectonics of the western Ordos Plateau, Ningxia, China: Slip rates on the Luoshan and East Helanshan Faults, Tectonics, 35, 2754–2777, which has been published in final form at https://doi.org/10.1002/2016TC004230. This article may be used for non-commercial purposes in accordance with Wiley Terms and Conditions for Self-Archiving.

# The tectonics of the western Ordos Plateau, Ningxia, China: slip rates on the Luoshan and East Helanshan Faults

Timothy A. Middleton,[1] Richard T. Walker,[1] Dylan H. Rood,[2] Edward J. Rhodes,[3] Barry Parsons,[1] Qiyun Lei,[4] Yu Zhou,[1] John R. Elliott,[1] and Zhikun Ren[5]

`Authors' manuscript, submitted version of paper published as:`
`Tectonics, 35, 2754–2777, doi:10.1002/2016TC004230`

**Key Points.**

- Here is the first keypoint. what happens if it is a long keypoint, like this one. We want to see this wrap please.
- This is the second.
- And here is the third keypoint

---

Corresponding author: Timothy A. Middleton, COMET, Department of Earth Sciences, University of Oxford, South Parks Road, Oxford, OX1 3AN, UK. (tim.middleton@earth.ox.ac.uk)

[1]COMET, Department of Earth Sciences,

**Abstract.**

Analysis of the locus, style and rates of faulting is fundamental to understanding the kinematics of continental deformation. The Ordos Plateau lies to the northeast of Tibet, within the India-Eurasia collision zone. Previous stud-

---

University of Oxford, South Parks Road,
Oxford, OX1 3AN, UK

[2]Department of Earth Science and
Engineering, Imperial College London,
South Kensington Campus, London SW7
2AZ, UK & AMS Laboratory, Scottish
Universities Environmental Research
Centre, East Kilbride G75 0QF, UK

[3]Department of Geography, University of
Sheffield, Sheffield, S10 2TN, UK

[4]Ningxia Seismological Bureau, Yinchuan,
China

[5]State Key Laboratory for Earthquake
Dynamics, Institute of Geology, China
Earthquake Administration, Beijing, China

ies have suggested that it behaves rigidly and rotates anticlockwise within a large-scale zone of ENE-WSW left-lateral shearing. For this rotation to be accommodated, the eastern and western margins of the Ordos Plateau should be undergoing right-lateral shearing and yet the dominant faulting style appears to be extensional. We focus specifically on the kinematics of the faults bounding the western margin of the Ordos Plateau and make new slip rate estimates for two of the major faults in the region: the right-lateral strike-slip Luoshan Fault and the normal-slip East Helanshan Fault. We use a combination of IRSL dating of offset landforms with high-resolution imagery and topography from the Pleiades satellites to determine an average right-lateral slip rate of 4.3±0.4 mm/a ($1\sigma$ uncertainties) on the Luoshan Fault. Similarly, we use $^{10}$Be exposure dating to determine a throw rate on the East Helanshan Fault of 0.8±0.1 mm/a, corresponding to an extension rate of 0.9±0.1 mm/a ($1\sigma$ uncertainties).

We therefore conclude that right-lateral shearing is the dominant motion occurring in the western Ordos region, supporting a kinematic model of large-scale anticlockwise rotation of the whole Ordos Plateau.

## 1. Introduction

Deformation on the continents tends to be distributed across broad networks of faults (e.g. *Thatcher* [2009]). For instance, in the India-Eurasia collision zone, 4 cm/a of relative motion is accommodated in a region spanning thousands of kilometres [*DeMets et al.*, 1990, 1994; *England and Molnar*, 1997; *Wang et al.*, 2001]. Within the India-Eurasia collision zone, though, there are also regions that appear not to deform. It is important to understand the active tectonics of such regions because non-deforming blocks tend to localise strain, and hence seismic hazard, at their margins (e.g. *Molnar and Dayem* [2010]), yet the style of faulting and rates of motion of these blocks are not always predictable from nearby plate velocities (e.g. *McKenzie and Jackson* [1983]; *Jackson and McKenzie* [1988]). For example, large-scale transtensional shearing can sometimes be accommodated purely by en-echelon normal faulting and vertical axis rotations of intervening crustal blocks [*Wesnousky et al.*, 2012].

The Ordos Plateau, which lies to the northeast of the Tibetan Plateau in northern central China, is one such apparently non-deforming region. It sits within the India-Eurasia collision zone—hence in a region of overall shortening—and yet large normal faults and extensional grabens are present along most of its boundaries, suggesting that the region is extending in all directions (see Figure 1). However, both geological and GPS measurements indicate that the Ordos Plateau is situated within a large, left-lateral shear zone and should be rotating anticlockwise about a vertical axis within this zone, indicating predominantly strike-slip motion at its edges [*Xu and Ma*, 1992; *Xu et al.*, 1993; *Avouac and Tapponnier*, 1993; *Xu et al.*, 1994; *Zhang et al.*, 1995; *Peltzer and*

*Saucier*, 1996; *Zhang et al.*, 1998; *Zhao et al.*, 2015] (see Figures 2 (a), 1 (b) and 1 (c)). Yet evidence for anticlockwise rotation of the Ordos Plateau is relatively sparse. *Xu et al.* [1994] used palaeomagnetic data to estimate a total anticlockwise rotation of 1.3 to 3.7° with respect to the Xinjiang region of northwest China since the Late Tertiary, corresponding to a rotation rate of 0.5 to 1.4°/Ma. However, their samples are from the deforming eastern margin of the Ordos Plateau (see Figure 1), and so are likely to be affected by local rotations within this deforming belt. Furthermore, *Li et al.* [2001] report much higher anticlockwise rotation rates of tens of degrees per million years, also on the basis of palaeomagnetic data (see Figure 1)—although their samples are also primarily from the deforming margins of the Ordos Plateau. *Fan and Ma* [2003] used the fairly sparse GPS dataset of *Wang et al.* [2001] (including only 6 sites on the Ordos Plateau) to estimate an anticlockwise rotation rate of 0.02°/Ma about a pole at 51.5°N, 120.1°E with respect to stable Eurasia.

If anticlockwise rotation about a vertical axis is important for the kinematics of the Ordos Plateau, we would expect to see dominantly right-lateral motion on both the eastern and western sides of the plateau as it rotates with respect to the Alxa Desert in the west and the North China Plain in the east (see Figure 1). On the eastern side of the Ordos Plateau it is known that right-lateral shearing occurs through normal faulting on the en-echelon Shanxi Grabens and right-lateral slip on the Xizhoushan Fault (at 5.7 mm/a) and the Huoshan Fault (at 7 mm/a) [*Xu et al.*, 1986; *Xu and Deng*, 1990] (see later Figure 19 for locations). On the western side of the Ordos Plateau, right-lateral faults are also identified, though their rates of motion and relative importance are debated (e.g. *Deng et al.* [1984]; *Min et al.* [1992, 1993]; *Zhang et al.* [1998]; *Min et al.* [2003]).

In this study we therefore examine the relative importance of right-lateral and extensional slip in the western Ordos region by determining Holocene rates for two of the major faults within the region: the Luoshan Fault (right-lateral strike-slip) and the East Helanshan Fault (normal). We then use our results to build a kinematic model of the Ordos Plateau that incorporates both anticlockwise rotation and the widespread normal faulting.

## 2. Tectonic setting

The western Ordos region straddles the transition from the shortening occurring in the northeastern corner of the Tibetan Plateau to the apparent extension occurring across the Yinchuan Graben. Many recent studies have indicated that deformation in northeast Tibet has accelerated since about 15 Ma ago and that the orientation of the regional stress field has changed since about 20 Ma ago (e.g. *Molnar and Stock* [2009]; *Yuan et al.* [2013] and references therein). Within the western Ordos region, apatite fission track dating reveals rapid uplift and exhumation of the Helanshan 10-12 Ma ago [*Liu et al.*, 2010] and the Liupanshan around 8 Ma ago [*Zheng et al.*, 2006] (see Figure 1). It seems likely that motions at the margins of the Ordos Plateau are sensitive to changes in the stress field in northeast Tibet and were initiated at a similar time (e.g. *Wang et al.* [2013]; *Chen et al.* [2015]).

Four large, historical earthquakes have occurred in the vicinity (see Figure 3): the 1561 M 7.3 earthquake near the Luoshan Fault [*Min et al.*, 2003]; the 1709 M 7.3 oblique left-lateral strike-slip-faulting Zhongwei earthquake [*Nie and Lin*, 1993; *Min et al.*, 2001]; the 1739 M 7.6 normal-faulting Yinchuan earthquake [*Liao and Pan*, 1982; *Zhang et al.*, 1986; *Deng and Liao*, 1996; *Bai and Jiao*, 2005; *Chai et al.*, 2006; *Lin et al.*, 2013; *Lei et al.*, 2015; *Lin et al.*, 2015; *Middleton et al.*, 2015]; and the 1920 M 8.5 left-lateral strike-slip-faulting Haiyuan earthquake [*Zhang et al.*, 1987, 1988; *Burchfiel et al.*, 1991; *Lasserre et al.*, 2002; *Liu-Zeng et al.*, 2007; *Ren et al.*, 2015].

The left-lateral Haiyuan Fault, with a Quaternary slip rate in the range of 5 to 10 mm/a [*Zhang et al.*, 1990; *Min et al.*, 2000; *Li et al.*, 2009], runs along the northeastern edge of the Tibetan Plateau and enters the southern part of Ningxia Province, on the western side of the Ordos Plateau, striking northwest-southeast and terminating in a series of reverse faults. These reverse faults form a south-trending fold-and-thrust zone that extends as far as the Liupanshan at the southernmost extent of the province [*Deng et al.*, 1984; *Li et al.*, 2013]. The M 8.5 1920 earthquake occurred on the easternmost part of the Haiyuan Fault [*Zhang et al.*, 1987; *Ren et al.*, 2015].

To the north of the Haiyuan Fault are three more sets of oblique reverse faults: the Tianjinshan-Miboshan Fault (also called the Zhongwei-Tongxin Fault), the Yantongshan Fault, and the Niushoushan and Luoshan Faults (see Figure 3). The existence and orientation of these ranges implies northeast-southwest crustal shortening, which is in agreement with modern GPS studies [*Gan et al.*, 2007; *Li et al.*, 2013]. The M 7.3 1709 Zhongwei earthquake is thought to have occurred on the Tianjinshan-Miboshan Fault.

The two faults that we examine in detail in this paper—the Luoshan right-lateral strike-slip fault and the East Helanshan normal fault—are discussed separately in Sections 4 and 5.

## 3. Methods

### 3.1. Pleiades data and DEM construction

We acquired Pleiades stereo imagery of the central portion of the Luoshan Fault (on 18th July 2014) and the southern portion of the East Helanshan Fault (on 23rd April and 17th July 2014). See Figure 3 for data coverage. We then constructed high-resolution digital elevation models (DEMs) of each region according to the methodology outlined in *Middleton et al.* [2015] and *Zhou et al.* [2015] (see also Supporting Information).

The resulting DEM for the Luoshan Fault has a horizontal resolution of 1 to 2 m (48% of 1 m by 1 m grid cells contain at least one point, whilst 74% of 2 m by 2 m grid cells contain at least one point). A surface roughness map was calculated from the DEM by finding the standard deviation of the slope in a 9×9 m moving window [*Frankel and Dolan*, 2007]. The resulting DEM for the southern end of the East Helanshan Fault has a horizontal resolution, at least around the scarps, of about 2 m [*Middleton et al.*, 2015]. Again, a surface roughness map was calculated, this time using a 5×5 m moving window as this window size was found to more clearly highlight the roughness contrast between different geomorphological surfaces [*Frankel and Dolan*, 2007].

For each region, we used the DEM in combination with the surface roughness data and the original imagery to map the fault scarps and geomorphology in detail, tying our remote sensing observations to our field investigations. For the southern end of the East

Helanshan Fault, we also calculated the 5th, 25th, 50th, 75th and 95th percentiles of the surface roughness raster for each of the mapped geomorphological units. The median roughness values show an initial decrease with age, followed by a slight increase for the oldest terrace. This agrees with the results of *Frankel and Dolan* [2007]: the initial bar and swale topography on the fan surface is smoothed over time by erosion, but eventually the surface is made rougher again by channel incision. All DEMs, surface roughness data and geomorphological maps are shown in later figures in the results sections.

### 3.2. Offset measurements

We measured vertical offsets across fault traces by drawing swath profiles across the raw point cloud data and fitting lines above and below the scarp. The quoted errors on our vertical offset measurements refer to the root mean square (RMS) residuals from this line fitting process. We determined horizontal offsets from the original Pleiades imagery by fitting straight lines (by eye) to offset geomorphological markers. We then measured the horizontal distance between the two piercing points, where these lines intersected our mapped fault trace. Unless otherwise stated, quoted errors on our horizontal offset measurements are $1\sigma$ standard deviations based on suites of measurements from sets of geomorphological features that appear to have been displaced by the same amount (according to our field observations). Full details of our methodologies are given in the Supporting Information and horizontal offset measurements are recorded in Table 1.

### 3.3. Quaternary dating of offset features

On the Luoshan Fault the fluvial sediments contained abundant silts and fine sand horizons, so we used infrared stimulated luminescence (IRSL) dating to constrain the ages of offset geomorphological features (unfortunately, radiocarbon dating was not possible due to the absence of datable material). Full details of the dating technique and sample preparation procedure are given in the Supporting Information, and the results are shown in Table 2. The quoted errors refer to $1\sigma$ analytical uncertainties propagated in quadrature unless otherwise stated.

On the East Helanshan Fault the alluvial fans comprise poorly consolidated, sub-angular gravels, pebbles, cobbles and boulders, with very little vegetation. The coarse grain size and lack of preserved organic material precluded dating by either radiocarbon or IRSL methods (with the exception of a few very recent deposits, which are well-exposed in modern river channels—see *Middleton et al.* [2015]). We therefore used $^{10}$Be exposure dating of boulder tops and suites of quartz pebbles to provide age constraints on the East Helanshan Fault. Background to the $^{10}$Be dating procedure and details of the sample preparation and analysis are included in the Supporting Information. The results are given in Table 4.

Again, the quoted errors refer to $1\sigma$ analytical uncertainties propagated in quadrature unless otherwise stated. A number of our $^{10}$Be ages are from amalgamated samples and in these cases we do not have any constraints on the spread of ages within the population of sampled clasts. It should be emphasised, therefore, that the errors on the amalgamated samples still refer to analytical uncertainties and not the standard deviations within the populations.

In order to calculate errors on our slip rate estimates we propagate fractional uncertainties from our offset measurements and our age results in quadrature. On the strike-slip

Luoshan Fault we report horizontal slip rates, whereas on the normal East Helanshan Fault we initially report throw rates because we do not have good constraints on the fault dip. However, on the northern, strike-slip section of the East Helanshan Fault (see Section 5.5) we again report horizontal slip rates.

## 4. The Luoshan Fault

### 4.1. Background

The Luoshan Fault is approximately 60 km long and runs along the eastern side of the Luoshan (Luo Mountains) [*Min et al.*, 2003]. The Luoshan comprise two ranges: the Daluoshan (Big Luo Mountains) to the north and the Xiaoluoshan (Small Luo Mountains) to the south, both of which are composed of Ordovician basement (see Figure 4). The Luoshan Fault was originally thought to be a left-lateral strike-slip fault [*The Research Group on "Active Fault System around Ordos Massif"*, 1988; *Zhang et al.*, 1990; *Zhou et al.*, 2000], but a detailed re-assessment found numerous examples of right-lateral offsets in Quaternary and Holocene material [*Min et al.*, 1992, 1993, 2003]. Evidence for recent, right-lateral motion is also seen further south on the Yunwushan Fault in the form of displaced river channels (for example at 36.635 °N, 106.349 °E and 36.531 °N, 106.333 °E—see Figure 3). *Min et al.* [2003] used two thermoluminescence (TL) ages to estimate a minimum, right-lateral slip rate on the Luoshan Fault since the Late Pleistocene of 2.15±0.20 mm/a. The fault is assigned a right-lateral rate of 3 mm/a on the *Map of Active Tectonics in China* [*Deng et al.*, 2004]. *Min et al.* [2003] also suggest that the 1561 M 7.3 earthquake occurred on the Luoshan Fault (see Figure 3) on the basis that comparatively young-looking gullies (1 m deep) record offsets of 1.5 to 5.4 m and that a free face is visible on some scarps, particularly near the village of Zhangjiashanpo (see Figure 4 (a) for location). Given the uncertainty about the kinematics of the Luoshan Fault and the paucity of slip rate constraints, we re-visit the fault in this study using up-to-date luminescence methods and modern satellite imagery.

At its northern end, the Luoshan Fault strikes at 353 ° and runs along the eastern side of the Luoshan mountains just west of Tanzhuangzicun (see Figure 4). Gullies draining these mountains dissect an alluvial apron, draining first to the east and then curving to the north to follow the local slope, and preserve evidence of right-lateral offsets. Moving south, the fault strike changes to 330 ° around the northern end of the Daluoshan. Surface offsets are harder to identify, but *Min et al.* [2003] found evidence of thrusting in this section. The fault then tracks south, with a strike of 358 °, cutting across at least four different generations of alluvial fans (F1-4, where F1 is the youngest and F4 is the oldest) emanating from the Daluoshan (see Figures 5 (a) and 5 (b)). The older fans are more heavily incised and the channels on these surfaces are more sinuous. The different generations of alluvial fans are evident on slope and roughness maps (see later Figures 9 (a) and 9 (b)). Multiple, parallel scarps are seen in this section, most of which include a component of uplift on their western side; the youngest fans preserve a vertical offset of $1.1\pm0.3$ m (see Figure 5 (b)). At the southern end of the Daluoshan section, the fault makes a small dog-leg to the southeast and forms a 5 to 10 m high, 500 m long pressure ridge at 37.240 °N, 106.322 °E.

Moving south again, the fault lies along the eastern side of the Xiaoluoshan with a strike of 342 °. It cuts across the heads of a number of alluvial fans, most of which appear to be of the same age on the basis of their colour and texture (for example, see Figures 5 (c) and 5 (d)). The streams draining the Xiaoluoshan preserve a number of examples of right-lateral offsets and the fans here are uplifted on the eastern side of the fault trace by 5.0±1.4 m (see Figure 5 (d)). The fault then continues in this orientation until the southern end of the Xiaoluoshan, 9 km south of Zhangjiashanpo. In addition, a series of 12 to 23 m high east-facing scarps are present east of the main strike-slip fault, between 106.34 °E and 106.39 °E (see Figure 4 (a)). We interpret these scarps to represent superficial spatial separation of strike-slip and reverse components of motion onto two parallel fault strands.

The smallest vertical offset (1.1±0.3 m), at 37.255 °N, 106.320 °E, was measured where the local fault strike is 003 ° (see Figure 5 (b)). Other sections of the fault, with more northwesterly strikes, showed larger vertical offsets indicating a greater amount of shortening. We therefore deduce that pure strike-slip motion occurs at an azimuth slightly east of 003 °.

Slip rate sites at Xiaoluoshan, Tanzhuangzicun, Shiyaodong and Machanggou are described separately below.

## 4.2. Xiaoluoshan section

### 4.2.1. Overview and offset measurement

Our first slip rate site on the Luoshan Fault is adjacent to the Xiaoluoshan (see Figure 4 (a)). Here, the fault cuts through an alluvial apron on the eastern side of the mountains and a large number of channels (approximately 300 m spacing) flow eastwards across the fault trace, draining the Xiaoluoshan. Almost all of these channels show evidence of tens of metres of right-lateral offset. There is also a small amount of uplift (approximately 5 m) on the eastern side of the fault trace (see Figure 5 (d)).

Given that the whole area appears to be covered by an alluvial apron composed of coalesced fans of the same age, we propose that all of the geomorphological markers should preserve the same offset. We measured the offsets preserved by nine different markers (six channel riser tops, one channel riser bottom and two channel thalwegs—see yellow lines in Figure 6 (b)) according to the methodology described in the Supporting Information and obtained a mean offset of 37.2±5.5 m and range of 29.2 to 44.4 m (see Table 1). Figures 6 (c) and 6 (d) show that a 37 m restoration aligns an indistinct riser on the western side of the fault trace with a more pronounced channel margin (from which IRSL sample 2 was taken) on the uplifted eastern side. At the site of IRSL sample 1, the right-lateral fault motion is superposed on a pre-existing channel meander so the horizontal offset is harder to determine. However, Figures 6 (e) and 6 (f) show that the 37 m restoration aligns both a channel thalweg to the south of the sampling site and a ridge crest adjacent to the site.

#### 4.2.2. Age constraints and slip rate

IRSL sample 2 was taken from a channel riser on the eastern side of the fault at 37.178 °N, 106.340 °E. The sample was from a patch of slightly coarser sand interbedded with fine-grained, brown loess at a depth of 55 cm. An angular gravel layer with 10 cm clasts is visible approximately 30 cm above the sample (see Figure 7 (b)), ensuring that we are dating material that was deposited prior to or during a fluvial regime, rather than aeolian deposits that have accumulated after fan abandonment. The IRSL sample returned an age of 9.2±0.6 ka (see Table 2).

IRSL sample 1 was taken from the same alluvial surface, 930 m to the northwest of IRSL sample 2, at 37.185 °N, 106.335 °E. The sample was taken from a fine-grained, brown loess

1.5 m below the ground surface. However, due to erosion at the site, this was estimated in the field to correspond to 2.1 m below the top of the adjacent alluvial fan. The sample was overlain by a coarser sand layer and at least two gravel layers with 5 cm, sub-angular clasts of dark, Palaeozoic bedrock (see Figure 6 (d)). The sample returned an age of 141±12 ka (see Table 2).

The mean offset (37 m) and the age of IRSL sample 2 allow us to calculate a minimum slip rate of 4.1±0.7 mm/a (see Table 3). Meanwhile, IRSL sample 1 indicates a minimum slip rate of 0.26±0.05 mm/a (see Table 3). IRSL sample 1 is from deeper in the stratigraphy than IRSL sample 2, and may therefore represent sediments from a period of fan aggradation older than the most recent fan-forming episode. These slip rate results are discussed further in Section 6.

## 4.3. Tanzhuangzicun section

### 4.3.1. Overview and offset measurement

Our second slip rate site on the Luoshan Fault is at its northern end, beyond the end of the Daluoshan and around 1.75 km west of the village of Tanzhuangzicun (see Figure 4 (a)). This section of the fault strikes at 355° and cuts across an alluvial apron into which a number of channels have been incised (see Figure 8 (a)). The alluvial surface itself has been modified and terraced for agriculture (see Figures 8 (b) and (c)) and some very young streams have developed on top of this modified surface. However, evidence for right-lateral fault motion has been preserved by the channel margins of the more heavily incised streams. The whole fan surface slopes gently to the north and so the channels are offset in the opposite direction to the regional gradient. We also see evidence of eroded corners of channel risers on the down-slope edges of the channels (see Figures 8 (d) and (e)) [e.g. *Cowgill* [2007]].

The mean offset recorded by ten different geomorphological markers (eight channel riser tops, one channel riser bottom and one channel thalweg) on this single alluvial surface was 50.6±6.7 m and range of 37.2 to 61.4 m (see Table 1). Figures 8 (d) and (e) show how a 51 m restoration aligns all of these markers, including those immediately adjacent to the site of IRSL sample 3.

#### 4.3.2. Age constraints and slip rate

IRSL sample 3 was taken at 37.425 °N, 106.280 °E, just to the east of the fault trace. The sample was from fairly homogeneous, fine, yellow-brown loess, 169 cm below the ground surface and approximately 15 cm below a thin gravel layer with 5 cm clasts of angular material (see Figure 8 (g)). The sample returned an age of 10.6±0.9 ka (see Table 2). The mean offset (51 m) and the age of IRSL sample 3 allow us to calculate a minimum slip rate along the Tanzhuangzicun section of 4.8±0.8 mm/a (see Table 3).

### 4.4. Shiyaodong site

#### 4.4.1. Overview and offset measurement

*Min et al.* [2003] used TL dates from two sites (Shiyaodong and Machanggou) at the southern end of the Daluoshan section to obtain their slip rate estimate (see Figure 5 (b)). Here we use the high-resolution Pleiades DEM and our geomorphological mapping to re-estimate the offsets at their sites.

At the southern end of the Daluoshan section, four different generations of alluvial fans can be identified on the basis of their surface texture and degree of incision (see Figures 9

(a) and 9 (b), which are of the same area as Figure 5 (b)). The Shiyaodong site is on the F3 surface and *Min et al.* [2003] measured an offset of 18±1 m. However, although an 18 m restoration at this site re-aligns nearby gullies on a younger terrace surface, it does not appear to re-align the gully that *Min et al.* [2003] sampled (see Figure 9 (d)). The restoration is also complicated by the fact that the channels on the F3 surface are highly sinuous, leading to a large degree of ambiguity in the amount of slip. However, we re-measured the horizontal offsets of five piercing lines for channel thalwegs incised into the F3 surface and obtained a mean offset of 41.1±5.9 m and range of 33.8 to 48.5 m (see Table 1 and Figures 9 (e) and 9 (f)).

#### 4.4.2. Age constraints and slip rate

At Shiyaodong (37.252 °N, 106.320 °E) *Min et al.* [2003] obtained a TL age of 9.80±0.75 ka for the F3 surface. Using our new offset measurement we therefore estimate a new slip rate of 4.2±0.7 mm/a (see Table 3).

### 4.5. Machanggou site

#### 4.5.1. Overview and offset measurement

At the Machanggou site, 1.7 km north of Shiyaodong (see Figure 5 (b)), *Min et al.* [2003] measured an offset of 171±10 m. However, according to our geomorphological mapping (see Figures 5 (b), 9 (a) and 9 (b)), the channel *Min et al.* [2003] investigated runs along the side of the F4 surface rather than being incised into it. Their measured offset may therefore not be representative of the displacement recorded by F4.

#### 4.5.2. Age constraints and slip rate

At Machanggou (37.267 °N, 106.321 °E), *Min et al.* [2003] obtained a TL age of 69.0±5.4 ka. However, their sample was from 3 m below the surface of F4 and so may well be significantly older than that last episode of deposition on this surface (as we interpreted for our IRSL sample 1). Due to the uncertainty in the offset measurement and age constraint at this site, we are not able to estimate a slip rate at Machanggou.

## 5. The East Helanshan Fault

### 5.1. Background

The Yinchuan Graben is sited at the northern end of Ningxia Province, where the deformation appears to be markedly different from that described for the Luoshan Fault. Four major northeast-southwest trending normal faults cut Cenozoic and Quaternary strata, accommodating apparently northwest-southeast extension. From west to east these faults are: the East Helanshan Fault, the Luhuatai Fault, the Yinchuan-Pingluo Fault, and the Yellow River Fault (see Figure 3).

The East Helanshan Fault is approximately 120 km long and runs along the eastern side of the Helanshan (Helan mountains). *Zhang et al.* [1990] estimate a Quaternary throw rate for the East Helanshan Fault of 0.5 to 0.8 mm/a on the basis of the thickness of Quaternary sediments in the basin. The throw rate on the Yellow River Fault is estimated from TL ages of offset river terraces to be around 0.23 to 0.25 mm/a [*Liao et al.*, 2000]. Throw rates on the Yinchuan-Pingluo and Luhuatai are estimated from composite drilling profiles to be 0.14 mm/a ($^{14}$C date) and 0.18 mm/a (luminescence date) respectively [*Lei et al.*, 2008, 2011, 2015]. According to a cross-sectional area balance, the whole Yinchuan Graben is thought to have extended at 2.9±1.0 mm/a since the Pliocene, though this result relies on the interpretation of seismic reflection profiles [*Zhang et al.*, 1998]. The graben contains 1 to 1.6 km of Quaternary sediments and approximately 6 km of pre-Quaternary deposits that have accumulated since the Late Eocene [*Zhang et al.*, 1990].

A series of fresh scarps are present along the East Helanshan Fault [*Liao and Pan*, 1982]. The southernmost section of these scarps is called the Suyukou scarps, which vary in strike between 10 and 50 ° and cut through four, large, coalesced, alluvial fans some 3 km from the range-front. From south to north, these fans are called the Baisikou, Suyukou, Helankou and Chaqikou Fans [*Deng and Liao*, 1996] (see Figure 10 (b)). *Deng and Liao* [1996] also identified four separate terrace levels in the scarp footwalls, from T1 (the youngest, typically 3 m high and thought to be from the 1739 Yinchuan earthquake) to T4 (the oldest, up to 11 m high). The Baisikou, Suyukou and Helankou Fans are mainly mantled by the T2 surface, with only scattered remnants of T3 and T4—although the T1 surface is found adjacent to currently active channels. The Chaqikou Fan comprises primarily the T1 and T2 surfaces. Landforms older than T4 are only preserved in a few small areas. Firstly, at the range-front, some older terraces are preserved adjacent to minor catchments. Secondly, north of the Chaqikou Fan, there is a remnant of a heavily incised terrace (coloured dark brown in Figure 10 (b)), which is cut by multiple fault scarps and pre-dates T4. We call this terrace T5.

On the basis of palaeoseismic trenching and radiocarbon dating at the Suyukou scarps (and further north on the East Helanshan Fault), *Deng and Liao* [1996] concluded that at least three earthquakes occurred on this fault prior to 1739: 2600 years ago, 4600-6300 years ago, and 8400 years ago. If these trench ages correlate with the terrace surfaces preserved in the alluvial fans, then the offsets measured on the terraces can be used to calculate a throw rate. *Deng and Liao* [1996] measure a combined terrace offset for the last three events of 8.4 m. Combined with an age for the antepenultimate event of 6300 years, this yields a throw rate of 1.3 mm/a. In this study, however, we seek to provide the first direct measurement of the Late Quaternary throw rate on the East Helanshan Fault by conducting $^{10}$Be dating of the terrace surfaces themselves and by making new vertical offset measurements from high-resolution topography.

## 5.2. T5 at the northern end of the Suyukou scarps

### 5.2.1. Overview and offset measurement

Our first throw-rate site is on T5, at the northern end of the Suyukou scarps (see Figure 11 and Figure 10 for location). Multiple fault scarps cut T5, all of which must have formed since the abandonment of this surface. Topographic profiles from the Pleiades DEM show a combined offset across all of these scarps of 19.4±1.1 m (see Figure 11 and the Supporting Information for methodology).

### 5.2.2. Age constraints and throw rate

A suite of eight quartz pebbles (samples 11A to 11H, from 38.783 °N, 106.140 °E) and an amalgamated sample of 53 smaller clasts (sample 10, from 38.784 °N, 106.134 °E) were taken for $^{10}$Be dating from the surface of T5 (see Figure 11) and the results are shown in Figure 12 (a) and Table 4. Five of the eight clasts are in relatively close agreement with the aggregate age of 221.5±3.9 ka. We therefore interpret the three younger clasts (samples 11A, 11D and 11E) as outliers. An amalgamated sample of 42 pebbles (sample 12) and two individual clasts (samples 13A and 13B) were taken from the modern river (at 38.777 °N, 106.129 °E, see Figure 11 for location) to estimate the inheritance in this particular system. We obtained $^{10}$Be ages of 27.5±0.7 ka for the amalgamated sample, and 64.3±1.2 ka and 8.0±0.4 ka respectively for the two clasts. Although the small number of samples indicate a large range in the inherited component, the inheritance is nonetheless much less than the ages from the T5 surface itself. A zero inheritance model gives a T5 age of 221.5±3.9 ka, whilst the largest measured inheritance (sample 13A) gives a T5 age of 157.2±4.1 ka. These ages correspond to vertical throw rates of 0.09±0.01 mm/a and 0.12±0.01 mm/a respectively (see Table 3). The large uncertainty in the inheritance therefore has little effect on the calculated throw rate.

## 5.3. Central Suyukou scarps

### 5.3.1. Overview and offset measurement

Our second sampling site is at a location where a major river from the Helanshan crosses the Suyukou scarps (see Figures 10, 13 (a) and 13 (b)). Here, the staircase pattern of aggradational footwall terraces proposed by *Deng and Liao* [1996] (see Figure 13 (e)) can be seen to the southwest of the current channel. These terraces are also partially evident in the surface roughness map (see Figure 13 (c)). Topographic profiles extracted from the Pleiades DEM confirm the stepped pattern, with heights for T1, T2 and T3 of 3.5±0.8 m, 5.2±0.5 m and 11.2±1.5 m respectively (see Figure 13 (d) and the Supporting Information for the full methodology).

### 5.3.2. Age constraints

$^{10}$Be samples 14, 15 and 16 (consisting of amalgamations of 47, 49 and 73 quartz pebbles respectively) were taken from T2, T3 and the modern river (see Figure 13 (b) and Table 4 for locations). They yielded ages of 18.5±0.5 ka for T2, 42.3±1.0 ka for T3 and 14.4±0.7 ka for the modern river. Correcting for inheritance gives a T2 age of 4.1±0.9 ka and a T3 age of 27.9±1.2 ka. However, individual clasts taken from T2 (samples 14A to 14C) varied in age between 8.7±0.3 and 78.0±1.5 ka (see Figure 12 (d)). Similarly, individual clasts from the modern river (samples 16A to 16D) had ages between 9.6±0.3 and 33.6±0.8 ka (see Figure 12 (e)).

These results suggest that there is significant variation in the magnitude of the inherited component and that the ages obtained are not sufficiently reliable to determine the precise timing of the earthquakes represented by T2 and T3. Nonetheless, the aggregate T3 age of 42.3±1.0 ka and the youngest clast from the modern river of 9.6±0.3 (i.e. our lowest measure of what the inheritance might be) give a T3 age of 32.7±1.1 ka that we can consider to be an upper bound. Combined with the vertical offset of 11.2±1.5 m, this suggests a minimum throw rate of 0.34±0.05 mm/a over the last 30 ka (see Table 3). The discrepancy between this and the 1.3 mm/a from the data of *Deng and Liao* [1996] could be because there is not a one-to-one correlation between the colluvial wedges in the trenches and the terraces preserved at the surface. Furthermore, our minimum throw rate on the central Suyukou scarps is larger than the 0.09 to 0.12 mm/a obtained for T5 over the last 200 ka (see Section 5.2), which is just along strike to the north. Assuming that any earthquakes uplifting T3 also uplifted T5, this implies an increase in the throw rate over time.

## 5.4. Helanshan range-front

### 5.4.1. Overview and offset measurement

Our third throw-rate site is at the Helanshan range-front, at the location indicated in Figure 10. Here, a boulder fan straddles the range-front fault and a terrace is preserved either side of the channel on the footwall side (see Figure 14). This terrace pre-dates T1-4. Topographic profiles extracted from the Pleiades DEM indicate that the terrace records an offset on the range-front fault of 24.0±4.0 m (see Figure 14 (e) and the Supporting Information for methodology).

### 5.4.2. Age constraints and throw rate

An amalgamated sample of 83 quartz pebbles (sample 9, from 38.736 °N, 106.012 °E) and a single boulder top (sample 1, from 38.736 °N, 106.011 °E) were collected from the terrace surface southwest of the channel (see Figure 14 (b) for locations). We were not able to collect more boulder top samples because there were very few large boulders with well-preserved desert varnish on top of the terrace. The samples yielded $^{10}$Be ages of 120.6±1.9 ka and 111.5±2.0 ka respectively. Despite the small number of samples, the relatively close agreement between the two gives us confidence that the aggregate age is reliable.

We use the aggregate age of 120.6±1.9 ka to calculate a vertical throw rate of 0.20±0.03 mm/a (see Table 3), which is a minimum rate because it does not account for inherited $^{10}$Be. If we allowed for a much larger inheritance (of 64.3±1.2 ka, as measured for sample 13A in a different catchment) we obtain a vertical throw rate of 0.43±0.07 mm/a (see Table 3). In other words, even though the uncertainty on the inheritance is large, the maximum throw rate is still small (less than 0.5 mm/a).

In addition, six boulder tops (samples 3 to 8) were collected from the boulder fan that straddles the range-front fault (see Figure 14 (b) and Table 4 for locations). Since no scarps are preserved in the boulder fan itself, it must post-date the most recent surface-rupturing event at this location. The boulder tops range in age from 8.2±1.1 ka to 38.3±1.4 ka (see Figure 12 (b)). A plot of $^{10}$Be exposure age against distance down slope from the fault trace shows that more distal samples have older exposure ages (see Figure 12 (c)). This suggests that the boulder fan has been generated in more than one event, with the most recent episode of deposition being restricted to near the apex of the fan. Samples 4, 5 and 6, all from near the apex of the fan, have ages of 13.1±0.9, 8.2±1.1 and 11.1±0.5 ka respectively, and we propose that these three ages represent the probable abandonment age of the boulder fan.

## 5.5. Northern end of the East Helanshan Fault

### 5.5.1. Overview and offset measurement

At the northern end of the East Helanshan Fault we found evidence for right-lateral motion (see Figure 3 for location). Here, three boulder ridges on top of an alluvial fan surface and an incised gully are right-laterally offset (see Figure 15). The scarp is fresh, with a free face, and this site is at the northernmost end of the rupture trace from the 1739 Yinchuan earthquake [*Middleton et al.*, 2015]. The incised channel is offset by 4 m (see Figures 15 (b) and 15 (c)), probably representing displacement in the 1739 event. The boulder ridges form indistinct linear markers, but the shadows at the sides of the boulder ridges are not completely aligned by a restoration of 4 m; our best visual restoration is at 16 m, though with visually estimated uncertainties of at least ±5 m (see Figure 15 (d)).

#### 5.5.2. Age constraints and slip rate

IRSL samples 4 and 5 were taken from an exposure in the wall of an incised river channel that cuts across the displaced fan (39.236 °N, 106.658 °E) at depths of 54 cm and 127 cm respectively. IRSL sample 4 was from a 10 cm thick lens of medium brown silt, covered by a 50 cm thick layer of large, poorly sorted cobbles (see Figure 15 (e)); IRSL sample 5 was from a stratigraphically lower, 20 cm thick layer of orange sand surrounded by coarse gravels and cobbles (see Figure 15 (f)). Sample 4 returned an age of 1.27±0.14 ka and sample 5 returned an age of 3.21±0.21 ka (see Table 2). These results are stratigraphically consistent.

The 1.27 ka age implies a horizontal slip rate of 12.6±4.2 mm/a (see Table 3), which appears unrealistically large. However, we note that both samples are taken from the fill of a channel between the boulder ridges, which might post-date abandonment of the fan itself. It is hence likely that both IRSL ages underestimate the deposition age of the underlying displaced boulder ridge.

## 6. Discussion

### 6.1. Rates of faulting along the western Ordos Plateau

Our key result from the Luoshan Fault is that the slip rate is comparatively large (i.e $>$ 4 mm/a), which shows that this fault is one of the principal active structures in the western Ordos region. The agreement between our slip rate results from IRSL samples 2 and 3 (to within their $1\sigma$ analytical errors) and our re-assessment of the Shiyaodong site indicate that the mean right-lateral Holocene slip rate on the Luoshan Fault is 4.3±0.4 mm/a (where the error now refers to the weighted standard deviation of the three slip rate estimates, see Table 3). Furthermore, at all three sites the fans were dated to approximately 10 ka ago (and the measured horizontal offsets are similar). This common age suggests that the deposition of these fans is principally controlled by climate.

On the East Helanshan Fault our major result is that the throw rate, and hence the extension rate, is comparatively small (i.e. $< 1$ mm/a). Since the Suyukou scarps run parallel to the Helanshan range-front, we add our maximum throw rate estimate from Suyukou (of $0.34 \pm 0.05$ mm/a) to our maximum throw rate estimate from the range-front (of $0.43 \pm 0.07$ mm/a) to obtain a Late Quaternary throw rate for the fault as a whole of $0.8 \pm 0.1$ mm/a (see Table 3). This is consistent with the Quaternary average of 0.5 to 0.8 mm/a from *Zhang et al.* [1990]. Using the shallowest fault dip found in the literature of $39^\circ$ (and hence giving the maximum possible extension rate for this throw rate), we find an extension rate across the East Helanshan Fault of $0.9 \pm 0.1$ mm/a (see Table 3). If we also include the throw rates and fault dips of the other faults within the graben (Yellow River Fault: 0.25 mm/a and $72^\circ$ [*Liao et al.*, 2000; *Fang et al.*, 2009]; Yinchuan-Pingluo Fault: 0.14 mm/a and $71^\circ$ [*Lei et al.*, 2008, 2015]; Luhuatai Fault: 0.18 mm/a and $60^\circ$ [*Fang et al.*, 2009; *Lei et al.*, 2011]) we obtain an extension rate across the whole graben of $1.2 \pm 0.1$ mm/a. Additionally, our suggested increase in throw rate on the Suyukou scarps (see Section 5.3) could indicate that motion is being transferred from the range-front fault to the Suyukou scarps in the alluvial fans—possibly in order to cut off a corner in the range-front and straighten the fault.

Campaign GPS measurements [*Zhao et al.*, 2015] also indicate that right-lateral shearing is the major motion occurring in the western Ordos region (see Figure 16). Figure 16 (a) shows the data from *Zhao et al.* [2015] with a best fitting rigid body rotation (about an Euler pole at 46 °N, 72 °W, estimated from the vectors within this region) subtracted from all of the vectors. This ensures that rotations associated with this rigid-body-like motion do not distort our slip rate estimates. We model the fault parallel interseismic motion across the Luoshan Fault as a buried screw dislocation in an elastic half-space using the formulation from *Savage and Burford* [1973], where the velocity $u$ at a perpendicular distance $x$ from the fault is given by $u = \frac{s}{\pi} tan^{-1}\left(\frac{x}{d}\right)$, where $s$ is the slip rate and $d$ is the locking depth. The density of data is not sufficient to provide an independent constraint on the locking depth, so we assume locking depths in the range of 10 to 20 km [*Wright et al.*, 2013] in order to calculate the distribution of possible slip rate estimates. In Figure 16 (b), the range of possible arctangent functions fitted to the data indicates a right-lateral slip rate on the Luoshan and northern Yunwushan Faults of 4.0±0.5 mm/a. Our geological slip rate of 4.3±0.4 mm/a agrees well with this geodetic rate. We also note that one GPS point lies noticeably to the west of our best fitting curves. This may indicate that the centre of the shear zone at depth is displaced to the west of the surface trace of the Luoshan Fault, but there is not enough data to reliably test this. Figure 16 (c) shows that, although the errors on the data are large, there is no resolvable fault-perpendicular motion along profile X-X′; significant crustal shortening only occurs further to the south of our profile. The data in Figure 16 (d), for profile Y-Y′ across the Yinchuan Graben, are more scattered than in Figure 16 (b). If we assume that all of the right-lateral motion is localised onto a single structure, we obtain a right-lateral slip-rate of 3.0±0.4 mm/a (allowing for the same 10 to 20 km range of locking depths).

However the scatter in the data suggests that it is more likely that right-lateral motion is distributed across a number of the buried faults within the Yinchuan Graben. In Figure 16 (e), the scatter in the data is again very large—and extension is barely resolvable—but we obtain a best fitting extension rate of 1.3±1.6 mm/a across the Yinchuan Graben. This is consistent with our Late Quaternary extension rate of 1.2±0.1 mm/a and also supports our suggestion that right-lateral motion is dominant over the extension in the Yinchuan Graben.

### 6.2. A geometric model for the western Ordos Plateau

We propose a geometric model in which the faults of the western Ordos Plateau accommodate principally north-south right-lateral shearing. This occurs on the Luoshan Fault in the south and is split between the Alxa Desert and East Helanshan Faults in the north (see Figure 17). Satellite imagery shows evidence of right-lateral displacements on the Alxa Desert Fault, but its slip rate is unknown (see Figure 17 (c)). Meanwhile, our observations of offset boulder ridges at the northern end of the East Helanshan Fault (see Section 5.5) provide evidence for the continuation of right-lateral motion up the western side of the Ordos Plateau north of the Yinchuan Graben. A Kostrov summation for the two largest earthquakes in northern Ningxia in the last 700 years indicates that north-south right-lateral motion is one of the most significant strains [*Wesnousky et al.*, 1984]. Furthermore, one of the few focal mechanisms from the instrumental record (for a M 5.2 event in 1988—see Figure 3) is also consistent with north-south right-lateral motion.

In addition, we suggest that the (oblique reverse) Niushoushan Fault accommodates transpression as the strike-slip faulting steps to the left and that the normal faulting in the Yinchuan Graben accommodates transtension as the strike-slip faulting steps to the right. The estimated slip vector for the most recent earthquake on the East Helanshan Fault appears to show pure normal motion [*Middleton et al.*, 2015]. We therefore speculate that the transtension in the Yinchuan Graben is partitioned between normal motion on the East Helanshan Fault and right-lateral strike-slip motion on one or more of the buried faults within the graben (i.e. the Luhuatai, Yinchuan-Pingluo or Yellow River Fault).

## 7. Implications for the kinematics of the Ordos block

In Section 1 we saw that the Ordos Plateau is situated within a large-scale zone of WNW-ESE left-lateral shearing. To the south and west of the plateau, this shearing is manifested as slip on the Haiyuan Fault at 5-10 mm/a [*Zhang et al.*, 1988, 1990; *Burchfiel et al.*, 1991; *Min et al.*, 2000; *Cavalié et al.*, 2008; *Li et al.*, 2009] (see also Figure 1 (b)), the West Qinling Fault at 2-3 mm/a [*Deng et al.*, 2004; *Harkins et al.*, 2010], and the Qinlingshan Fault at 5-9 mm/a [*Zhang et al.*, 1995; *Deng et al.*, 2004]; to the north there is geological and geodetic evidence for around 2 mm/a of left-lateral motion on the Zhangjiakou-Bohai Fault system [*Zheng et al.*, 1981; *Xu et al.*, 1993; *Shen et al.*, 2000] (see Figure 19). Several kinematic models have proposed that the Ordos Plateau is rotating anticlockwise within this zone of shearing [*Xu and Ma*, 1992; *Xu et al.*, 1993; *Avouac and Tapponnier*, 1993; *Xu et al.*, 1994; *Zhang et al.*, 1995; *Peltzer and Saucier*, 1996; *Zhang et al.*, 1998].

We have shown that the anticlockwise rotation of the Ordos block can be confirmed by considering the fault kinematics at the boundary of the block. For an equidimensional crustal block that is rotating within a large-scale shear zone, the second order strike-slip motion on either side of the block is expected to be of a similar magnitude and opposite sense to the overall shear gradient across the block (see Supporting Information for mathematical details). In the case of the Ordos Plateau, the GPS data in Figure 18 (a) indicate an overall left-lateral shear gradient across the block of $\approx 5$ mm/a. Meanwhile, we have shown in this study that the dominant motion on the western side of the block is right-lateral, at a rate of $\approx 4$ mm/a. Right-lateral shearing also occurs on the eastern side of the block by normal slip on the en-echelon Shanxi Grabens and right-lateral slip on the Xizhoushan Fault (at 5.7 mm/a) and the Huoshan Fault (at 7 mm/a) [*Xu et al.*, 1986; *Xu and Deng*, 1990]. In other words, the Ordos Plateau behaves as expected, with the second order strike-slip motion on either side of the block occurring at a similar rate but in the opposite sense to the motion of the overall shear zone.

Figure 19 illustrates our kinematic model. The dotted lines in Figure 19 (a) indicate the possible existence of the Taihangshan and North China Plain blocks to the east of the Ordos Plateau. Little is known about the faulting to the west of the Ordos Plateau, but a series of mapped left-lateral faults in the Alxa Desert could be accommodating distributed shearing. Figures 19 (b), 19 (c) and 19 (d) show schematic representations of the kinematics, in which three blocks are rotating anticlockwise within a WNW-ESE left-lateral shear zone. For the rotations to be accommodated, either compression must occur at the NE and SW corners of each block, or the overall zone has to widen. For left-lateral shear at 5 mm/a, a kinematic model with equidimensional crustal blocks predicts widening of the zone at a rate of 1.8 mm/a (see Supporting Information for mathematical details).

The 1998 $M_w$ 5.7 Zhangbei earthquake had a reverse-faulting mechanism and occurred near the northeastern corner of the Ordos Plateau [*Li et al.*, 2008]—see Figure 19 (a). This event could therefore represent part of the compression necessary for anticlockwise rotation of the Ordos Plateau. However, the GPS data in Figure 18 (b) indicate NNE-SSW extension across the whole zone of 1.9±0.8 mm/a. This is in close agreement with the prediction of the kinematic model and therefore suggests that widening of the zone is the dominant mechanism allowing rotation.

Figures 19 (e) and 19 (f) show how the geometry of the system can be modified to account for the fact that the slip rate on the Haiyuan Fault is notably larger than that on the West Qinling Fault, thereby providing a possible explanation for the development of the Liupanshan. Figures 19 (g) and (h) show how initially corrugated block boundaries (as perhaps determined by the location of pre-existing structures) can lead to the development of en-echelon grabens and intervening right-lateral faults on the eastern and western margins of the block. (Faults in both the Yinchuan Graben and the Shanxi Grabens are known to have reactivated pre-existing structures [*Xu and Ma*, 1992; *Xu et al.*, 1993; *Liu*, 2000; *Darby and Ritts*, 2002].) Figures 19 (i) and (j) combine the above modifications into a single schematic representation of the kinematics.

Similar tectonic arrangements of rotating crustal blocks are also seen elsewhere—for example in northern Israel [*Ron et al.*, 1984], eastern Iran [*McKenzie and Jackson*, 1983; *Walker and Jackson*, 2004], the Walker Lane of western North America [*Wesnousky*, 2005; *Wesnousky et al.*, 2012], and the southeastern Tibetan Plateau [*Copley*, 2008]. The apparent predominance of normal faulting around the margins of the Ordos Plateau disguises the fact that it is the strike-slip motions that are most important. The normal faulting is present either as part of a partitioned transtensional system (as may be the case for the East Helanshan Fault) or because it is arranged en echelon to accommodate an overall shear (as is the case in the Shanxi Grabens—see also *Goldsworthy et al.* [2002]; *Wesnousky* [2005]). This is a similar situation to that suggested for the northern Walker Lane [*Wesnousky et al.*, 2012], though the shearing is in the opposite sense.

## 8. Conclusions

In the absence of reliable palaeomagnetic constraints, we have used the fault kinematics in the western Ordos region to examine the hypothesis that the Ordos block acts as a rigid crustal block within a large-scale left-lateral shear zone, rotating anticlockwise about a vertical axis. Our key result is that the rate of strike-slip motion on the Luoshan Fault (4.3±0.4 mm/a) is substantially larger than the throw rate on the normal East Helanshan Fault (0.8±0.1 mm/a). We therefore conclude that north-south right-lateral shearing is the principal tectonic motion in the western Ordos region, which is compatible with anticlockwise rotation of the whole Ordos block.

**Acknowledgments.**

This research has been supported by the Natural Environment Research Council (NERC) through a studentship awarded to TAM, the Centre for Observation and Modelling of Earthquakes, Volcanoes and Tectonics (COMET, GA/13/M/031), the Looking inside the Continents from Space (LiCS) large grant (NE/K011006/1), the NERC/ESRC Earthquakes without Frontiers (EwF) consortium (EwF_NE/J02001X/1_1), the National

Natural Science Foundation of China (41472201), and the State Key Laboratory of Earthquake Dynamics (LED2014A03).

We are grateful to: Peizhen Zhang and colleagues at the China Earthquake Administration (CEA) for assistance with fieldwork; Victoria Forbes, Maria Miguens-Rodriguez, Kathy Keefe and Owen Green for their help preparing the $^{10}$Be samples for dating; Rob Ashurst for his assistance with the IRSL dating; and Al Sloan, Austin Elliott and David Mackenzie for helpful discussions.

The Pleiades topography can be downloaded from OpenTopography (http://www.opentopography.org/). Most of the figures in this paper were made using GMT [*Wessel et al.*, 2013].

## References

**References**

Avouac, J.-P., and P. Tapponnier (1993), Kinematic model of active deformation in central Asia, *Geophysical Research Letters*, *20*(10), 895, doi:10.1029/93GL00128.

Bai, M., and D. Jiao (2005), The historical analysis for M=8 earthquake in 1739 at Yinchuan-Pingluo area, *Northwestern Seismological Journal*, *27*(2), 135–140 (in Chinese).

Balco, G., J. O. Stone, N. a. Lifton, and T. J. Dunai (2008), A complete and easily accessible means of calculating surface exposure ages or erosion rates from 10Be and 26Al measurements, *Quaternary Geochronology*, *3*(3), 174–195, doi:10.1016/j.quageo.2007.12.001.

Burchfiel, B. C., P. Zhang, Y. Wang, W. Zhang, F. Song, Q. Deng, P. Molnar, L. Royden, and L. Royden (1991), Geology of the Haiyuan Fault zone, Ningxia-hui autonomous region, China, and its relation to the evolution of the northeastern margin of the Tibetan Plateau, *Tectonics*, *10*(6), 1091–1110.

Cavalié, O., C. Lasserre, M.-P. Doin, G. Peltzer, J. Sun, X. Xu, and Z.-K. Shen (2008), Measurement of interseismic strain across the Haiyuan fault (Gansu, China), by InSAR, *Earth and Planetary Science Letters*, *275*, 246–257, doi:10.1016/j.epsl.2008.07.057.

Chai, C., G. Meng, P. Du, Y. Wang, B. Liu, W. Shen, Q. Lei, Y. Liao, C. Zhao, S. Feng, X. Zhang, and X. Xie (2006), Comprehensive multi-level exploration of buried active fault: an example of Yinchuan buried active fault, *Seismology and Geology*, *28*(4), 536–546 (in Chinese).

Chen, H., J. Hu, W. Gong, R. Kang, and L. Li (2015), Characteristics and transition mechanism of late Cenozoic structural deformation within the NiushoushanLuoshan fault zone at the northeastern margin of the Tibetan Plateau, *Journal of Asian Earth Sciences*, doi:10.1016/j.jseaes.2015.06.034.

Copley, A. (2008), Kinematics and dynamics of the southeastern margin of the Tibetan Plateau, *Geophysical Journal International*, *174*, 1081–1100, doi:10.1111/j.1365-246X.2008.03853.x.

Cowgill, E. (2007), Impact of riser reconstructions on estimation of secular variation in rates of strike slip faulting: Revisiting the Cherchen River site along the Altyn Tagh Fault, NW China, *Earth and Planetary Science Letters*, *254*, 239–255, doi:10.1016/j.epsl.2006.09.015.

Darby, B., B. Ritts, Y. Yue, and Q. Meng (2005), Did the Altyn Tagh fault extend beyond the Tibetan Plateau?, *Earth and Planetary Science Letters*, *240*(2), 425–435, doi:10.1016/j.epsl.2005.09.011.

Darby, B. J., and B. D. Ritts (2002), Mesozoic contractional deformation in the middle of the Asian tectonic collage: the intraplate Western Ordos foldthrust belt, China, *Earth and Planetary Science Letters*, *205*(1-2), 13–24, doi:10.1016/S0012-821X(02)01026-9.

DeMets, C., R. G. Gordon, D. F. Argus, and S. Stein (1990), Current plate motions, *Geophysical Journal International*, *101*(2), 425–478, doi:10.1111/j.1365-246X.1990.tb06579.x.

DeMets, C., R. G. Gordon, D. F. Argus, and S. Stein (1994), Effect of recent revisions to the geomagnetic reversal time scale on estimates of current plate motions, *Geophysical Research Letters*, *21*(20), 2191–2194.

Deng, Q., and Y. Liao (1996), Paleoseismology along the range-front fault of Helan Mountains, north central China, *Journal of Geophysical Research*, *101*, 5873–5893.

Deng, Q., F. Sung, S. Zhu, M. Li, T. Wang, W. Zhang, B. C. Burchfiel, P. Molnar, and P. Zhang (1984), Active faulting and tectonics of the Ningxia-Hui autonomous region, China, *Journal of Geophysical Research*, *89*, 4427–4445.

Deng, Q., Y. Ran, X. Yang, W. Min, and Q. Chu (2004), Map of Active Tectonics in China (in Chinese).

Ekström, G., M. Nettles, and A. Dziewonski (2012), The global CMT project 2004–2010: Centroid-moment tensors for 13,017 earthquakes, *Physics of the Earth and Planetary Interiors*, *200-201*, 1–9, doi:10.1016/j.pepi.2012.04.002.

England, P., and P. Molnar (1997), The field of crustal velocity in Asia calcualted from Quaternary rates of slip on Faults, *Geophysical Journal International*, *130*, 551–582.

Fan, J., and J. Ma (2003), Movement of Ordos block and alternation of activity along its boundaries, *Science in China (Series D)*, *46*(October), 168–180, doi:10.1360/03dz0013.

Fang, S., C. Zhao, C. Chai, B. Liu, S. Feng, M. Liu, Q. Lei, and H. Liu (2009), Seismological Evidences of the Crustal Structures and Tectonics in the Yinchuan Downfaulted Basin, *Chinese Journal of Geophysics*, *52*(5), 1101–1110, doi:10.1002/cjg2.1435.

Farr, T. G., P. A. Rosen, E. Caro, R. Crippen, R. Duren, S. Hensley, M. Kobrick, M. Paller, E. Rodriguez, L. Roth, D. Seal, S. Shaffer, J. Shimada, J. Umland, M. Werner, M. Oskin, D. Burbank, and D. Alsdorf (2007), The Shuttle Radar Topography Mission, *Reviews of Geophysics*, *45*, 1–33, doi:10.1029/2005RG000183.1.INTRODUCTION.

Frankel, K. L., and J. F. Dolan (2007), Characterizing arid region alluvial fan surface roughness with airborne laser swath mapping digital topographic data, *Journal of Geophysical Research: Earth Surface*, *112*(2), 1–14, doi: 10.1029/2006JF000644.

Gan, W., P. Zhang, Z.-K. Shen, Z. Niu, M. Wang, Y. Wan, D. Zhou, and J. Cheng (2007), Present-day crustal motion within the Tibetan Plateau inferred from GPS measurements, *Journal of Geophysical Research*, *112*(B8), 1–14, doi: 10.1029/2005JB004120.

Goldsworthy, M., J. Jackson, and J. Haines (2002), The continuity of active fault systems in Greece, *Geophysical Journal International*, *148*(3), 596–618, doi:10.1046/j.1365-246X.2002.01609.x.

Harkins, N., E. Kirby, X. Shi, E. Wang, D. Burbank, and F. Chun (2010), Millennial slip rates along the eastern Kunlun fault: Implications for the dynamics of intracontinental deformation in Asia, *Lithosphere*, *2*(4), 247–266, doi:10.1130/L85.1.

International Seismological Centre (2013), On-Line Bulletin.

Jackson, J., and D. McKenzie (1988), The relationship between plate motions and seismic moment tensors, and the rates of active deformation in the Mediterranean and Middle East, *Geophysical Journal International*, *93*(1), 45–73, doi:10.1111/j.1365-246X.1988.tb01387.x.

Lal, D. (1991), Cosmic ray labeling of erosion surfaces: in situ nuclide production rates and erosion models, *Earth and Planetary Science Letters*, *104*, 424–439.

Lasserre, C., Y. Gaudemer, P. Tapponnier, A.-S. Mériaux, J. Van der Woerd, Y. Daoyang, F. Ryerson, R. Finkel, and M. Caffee (2002), Fast late Pleistocene slip rate on the Leng Long Ling segment of the Haiyuan fault, Qinghai, China, *Journal of Geophysical Research*, *107*, doi:10.1029/2000JB000060.

Lei, Q., C. Chai, G. Meng, P. Du, Y. Wang, X. Xie, and X. Zhang (2008), Composite drilling section exploration of Yinchuan Buried Fault, *Seismology and Geology*, *30*(1), 250–263 (in Chinese).

Lei, Q., C. Chai, P. Du, Y. Wang, and G. Meng (2011), Activity characteristics of Luhuatai Buried Fault since Late Quaternary revealed by drilling, *Seismology and Geology*, *33*(3), 602–614 (in Chinese).

Lei, Q., C. Chai, P. Du, J. Yu, X. Xie, and Y. Wang (2015), Re-discussion of the seismogenic structure of the M8.0 Pingluo earthquake in 1739, *Seismology and Geology*, *37*(2), (in Chinese).

Li, C., P. Zhang, J. Yin, and W. Min (2009), Late Quaternary left-lateral slip rate of the Haiyuan fault, northeastern margin of the Tibetan Plateau, *Tectonics*, *28*, doi:10.1029/2008TC002302.

Li, W., Y. Lu, and G. Ding (2001), Paleomagnetic evidence from loess for the relative motion between the Ordos and its adjacent blocks, *Quaternary Sciences*, *21*(6), 551–559 (in Chinese).

Li, W., Y. Dong, A. Guo, X. Liu, and D. Zhou (2013), Chronology and tectonic significance of Cenozoic faults in the Liupanshan Arcuate Tectonic Belt at the northeastern margin of the QinghaiTibet Plateau, *Journal of Asian Earth Sciences*, *73*, 103–113, doi:10.1016/j.jseaes.2013.04.026.

Li, Z., W. Feng, Z. Xu, P. Cross, and J. Zhang (2008), The 1998 Mw 5.7 Zhangbei-Shangyi (China) earthquake revisited: A buried thrust fault revealed with interferometric synthetic aperture radar, *Geochemistry Geophysics Geosystems*, *9*(4), 1–11, doi:10.1029/2007GC001910.

Liao, Y., and Z. Pan (1982), Dislocation of the great wall in the Hongguozigou, Ningxia autonomous region, *Seismology and Geology*, *4*(2), 77–80 (in Chinese).

Liao, Y., C. Chai, W. Zhang, and W. Xu (2000), The active features and slip rate of Lingwu faults in late Quaternary, *Earthquake Research in China*, *16*(2), 158–165.

Lin, A., G. Rao, J. Hu, and W. Gong (2013), Reevaluation of the offset of the Great Wall associated with the ca. M 8.0 Pingluo earthquake of 1739, Yinchuan graben, China, *Journal of Seismology*, *17*(4), 1281–1294, doi:10.1007/s10950-013-9391-2.

Lin, A., J. Hu, and W. Gong (2015), Active normal faulting and the seismogenic fault of the 1739 M 8.0 Pingluo earthquake in the intracontinental Yinchuan Graben, China, *Journal of Asian Earth Sciences*, *114*, 155–173, doi: 10.1016/j.jseaes.2015.04.036.

Liu, G. (2000), The Cenozoic rift system of the North China Plain and the deep internal process, *Tectonophysics*, *133* (1987), 277–285.

Liu, J., P. Zhang, D. Zheng, J. Wan, W. Wang, P. Du, and Q. Lei (2010), Pattern and timing of late Cenozoic rapid exhumation and uplift of the Helan Mountain, China, *Science China Earth Sciences*, *53* (3), 345–355, doi:10.1007/s11430-010-0016-0.

Liu, M., S. Stein, and H. Wang (2011), 2000 years of migrating earthquakes in North China: How earthquakes in midcontinents differ from those at plate boundaries, *Lithosphere*, *3* (2), 128–132, doi:10.1130/L129.1.

Liu-Zeng, J., Y. Klinger, X. Xu, C. Lasserre, G. Chen, W. Chen, P. Tapponnier, and B. Zhang (2007), Millennial recurrence of large earthquakes on the Haiyuan fault near Songshan, Gansu Province, China, *Bulletin of the Seismological Society of America*, *97* (1B), 14–34, doi:10.1785/0120050118.

McKenzie, D., and J. Jackson (1983), The relationship between strain rates, crustal thickening, palaeomagnetism, finite strain and fault movements within a deforming zone, *Earth and Planetary Science Letters*, *65* (1), 182–202, doi:10.1016/0012-821X(83)90198-X.

Middleton, T. A., R. T. Walker, B. Parsons, Q. Lei, Y. Zhou, and Z. Ren (2015), A major, intraplate, normal-faulting earthquake: the 1739 Yinchuan event in northern China, *Journal of Geophysical Research (Solid Earth)*, *121* (1), 293–320, doi:10.1002/2015JB012355.Received.

Min, W., Z. Chai, P. Wang, P. Yang, C. Chai, P. Wang, and P. Yang (1992), Preliminary study on the Holocene active fault features at the eastern piedmont of the Luoshan mountain, *Earthquake Research in China*, *8* (4), 49–54 (in Chinese).

Min, W., Z. Chai, P. Wang, and P. Yang (1993), The study on the paleoearthqukes on the eastern piedmont fault of the Luoshan mountains in Holocene, *Earthquake Research in China*, *5* (4), 97–102 (in Chinese).

Min, W., P.-Z. Zhang, and Q.-D. Deng (2000), Primary study on regional paleoearthquake recurrence behavior, *Acta Seismologica Sinica*, *13* (2), 180–188, doi:10.1007/s11589-000-0008-9.

Min, W., P. Zhang, and Q. Deng (2001), The study of Holocene paleoearthquakes on Zhongwei-Tongxin fault zone, *Seismology and Geology*, *23* (3), 357–366 (in Chinese).

Min, W., D. Jiao, C. Chai, P. Zhang, and F. Mao (2003), Characteristics of the active Luoshan Fault since Late Pleistocene, North Central China, *Annals of Geophysics*, *46* (5), 997–1013.

Molnar, P., and K. E. Dayem (2010), Major intracontinental strike-slip faults and contrasts in lithospheric strength, *Geosphere*, *6* (4), 444–467, doi:10.1130/GES00519.1.

Molnar, P., and J. Stock (2009), Slowing of India's convergence with Eurasia since 20 Ma and its implications for Tibetan mantle dynamics, *Tectonics*, *28*, doi:10.1029/2008TC002271.

Nie, Z., and W. Lin (1993), Middle segment of Zhongwei-Tongxin fault zone: seismic deformation band of 1709 earthquake with M 7.5 along Xiangshan-Tianjingshan fault zone, *Earthquake*, pp. 41–44 (in Chinese).

Peltzer, G., and F. Saucier (1996), Present-day kinematics of Asia derived from geologic fault rates, *Journal of Geophysical Research*, *101*, 27,943–27,956, doi:10.1029/96JB02698.

Ren, Z., Z. Zhang, T. Chen, S. Yan, J. Yin, P. Zhang, W. Zheng, H. Zhang, and C. Li (2015), Clustering of offsets on the Haiyuan fault and their relationship to paleoearthquakes, *Geological Society of America Bulletin*, (June), doi:10.1130/B31155.1.

Ron, H., R. Freund, Z. Garfunkel, and A. Nur (1984), Block rotation by strike-slip faulting: structural and paleomagnetic evidence, *Journal of Geophysical Research*, *89* (B7), 6256–6270, doi:10.1029/JB089iB07p06256.

Savage, J. C., and R. O. Burford (1973), Geodetic determination of relative plate motion in central California, *Journal of Geophysical Research*, *78* (5), 832–845.

Shen, Z., C. Zhao, A. Yin, Y. Li, D. D. Jackson, P. Fang, and D. Dong (2000), Contemporary crustal deformation in east Asia constrained by Global Positioning System measurements, *Journal of Geophysical Research*, *105*, 5721–5734.

Stone, J. O. (2000), Air pressure and cosmogenic isotope production, *Journal of Geophysical Research*, *105* (B10), 23,753–23,759.

Tapponnier, P., and P. Molnar (1977), Active faulting and tectonics in China, *Journal of Geophysical Research*, *82* (20), 2905–2930.

Thatcher, W. (2009), How the Continents Deform : The Evidence From Tectonic Geodesy, *Annual Review of Earth and Planetary Sciences*, *37*, 237–262, doi:10.1146/annurev.earth.031208.100035.

The Research Group on "Active Fault System around Ordos Massif" (1988), *Active Fault System around Ordos Massif*, (in Chinese) pp., State Seismological Bureau, Seismological Press, Beijing.

Walker, R., and J. Jackson (2004), Active tectonics and late Cenozoic strain distribution in central and eastern Iran, *Tectonics*, *23* (5), doi:10.1029/2003TC001529.

Wang, Q., P. Z. Zhang, J. T. Freymueller, R. Bilham, K. M. Larson, X. Lai, X. You, Z. Niu, J. Wu, Y. Li, J. Liu, Z. Yang, and Q. Chen (2001), Present-day crustal deformation in China constrained by global positioning system measurements, *Science (New York, N.Y.)*, *294*, 574–7, doi:10.1126/science.1063647.

Wang, T., J. Zhuang, T. Kato, and M. Bebbington (2013), Assessing the potential improvement in short-term earthquake forecasts from incorporation of GPS data, *Geophysical Research Letters*, *40* (February), n/a–n/a, doi:10.1002/grl.50554.

Wesnousky, S. G. (2005), Active faulting in the Walker Lane, *Tectonics*, *24* (3), 1–35, doi:10.1029/2004TC001645.

Wesnousky, S. G., L. M. Jones, C. H. Scholz, and Q. Deng (1984), Historical seismicity and rates of crustal deformation along the margins of the Ordos block, North China, *Bulletin of the Seismological Society of America*, *74* (5), 1767–1783.

Wesnousky, S. G., J. M. Bormann, C. Kreemer, W. C. Hammond, and J. N. Brune (2012), Neotectonics, geodesy, and seismic hazard in the Northern Walker Lane of Western North America: Thirty kilometers of crustal shear and no strike-slip?, *Earth and Planetary Science Letters*, *329-330*, 133–140, doi:10.1016/j.epsl.2012.02.018.

Wessel, P., W. H. F. Smith, R. Scharroo, J. Luis, and F. Wobbe (2013), Generic Mapping Tools: Improved Version Released, *Eos, Transactions American Geophysical Union*, *94*(45), 409–410, doi:10.1002/2013EO450001.

Wright, T. J., J. R. Elliott, H. Wang, and I. Ryder (2013), Earthquake cycle deformation and the Moho: Implications for the rheology of continental lithosphere, *Tectonophysics*, *609*, 504–523, doi:10.1016/j.tecto.2013.07.029.

Xu, X., and Q. Deng (1990), The features of late Quaternary activity of the piedmont fault of Mt. Huoshan, Shanxi province and 1303 Hongdong earthquake (Ms=8), *Seismology and Geology*, *12*(1), 21–32 (in Chinese).

Xu, X., and X. Ma (1992), Geodynamics of the Shanxi Rift system, China, *Tectonophysics*, *208*(1-3), 325–340, doi: 10.1016/0040-1951(92)90353-8.

Xu, X., Q. Deng, and H. You (1986), Evidence on dextral dislocation of fault at the western foothills of Mt. Xizhoushan, Shanxi province and its slip rate during the Holocene, *Seismology and Geology*, *8*(3), 44–46 (in Chinese).

Xu, X., X. Ma, and Q. Deng (1993), Neotectonic activity along the Shanxi rift system, China, *Tectonophysics*, *219*(4), 305–325, doi:10.1016/0040-1951(93)90180-R.

Xu, X., G. Cheng, X. Ma, Y. Sun, and Z. Han (1994), Rotation model and dynamics of blocks in north China and its adjacent areas, *Earth Science - Journal of China University of Geosciences*, *19*(2), 129–138 (in Chinese).

Yu, S. (2004), A study on characteristics of tectonic block motion and tectonic setting of strong earthquakes in northern part of the Shanxi fault depression zone, *Acta Seismologica Sinica*, *17*(4), 417–425, doi:10.1007/s11589-004-0021-5.

Yuan, D.-Y., W.-P. Ge, Z.-W. Chen, C.-Y. Li, Z.-C. Wang, H.-P. Zhang, P.-Z. Zhang, D.-W. Zheng, W.-J. Zheng, W. H. Craddock, K. E. Dayem, A. R. Duvall, B. G. Hough, R. O. Lease, J.-D. Champagnac, D. W. Burbank, M. K. Clark, K. a. Farley, C. N. Garzione, E. Kirby, P. Molnar, and G. H. Roe (2013), The growth of northeastern Tibet and its relevance to large-scale continental geodynamics: A review of recent studies, *Tectonics*, *32*(5), 1358–1370, doi:10.1002/tect.20081.

Zhang, B., Y. Liao, S. Guo, R. E. Wallace, R. C. Bucknam, and T. C. Hanks (1986), Fault scarps related to the 1739 earthquake and seismicity of the Yinchuan Graben, Ningxia Huizu Zizhiqu, China, *Bulletin of the Seismological Society of America*, *76*(5), 1253–1287.

Zhang, P., P. Molnar, B. C. Burchfiel, and L. Royden (1988), Bounds on the Holocene slip rate of the Haiyuan Fault, north-central China, *Quaternary Research*, *30*, 151–164.

Zhang, P., B. C. Burchfiel, P. Molnar, W. Zhang, D. Jiao, Q. Deng, Y. Wang, L. Royden, and F. Song (1990), Late Cenozoic tectonic evolution of the Ningxia-Hui Autonomous Region, China, *Geological Society of America Bulletin*, *102*(11), 1484–1498, doi:10.1130/0016-7606(1990)102¡1484.

Zhang, W., D. Jiao, P. Zhang, P. Molnar, B. C. Burchfiel, Q. Deng, Y. Wang, and F. Song (1987), Displacement along the Haiyuan Fault associated with the great 1920 Haiyuan, China, earthquake, *Bulletin of the Seismological Society of America*, *77*(1), 117–131.

Zhang, Y., J. L. Mercier, and P. Vergely (1998), Extension in the graben systems around the Ordos (China), and its contribution to the extrusion tectonics of south China with respect to Gobi-Mongolia, *Tectonophysics*, *285*, 41–75.

Zhang, Y. Q., P. Vergely, and J. Mercier (1995), Active faulting in and along the Qinling Range (China) inferred from SPOT imagery analysis and extrusion tectonics of south China, *Tectonophysics*, *243*, 69–95.

Zhao, B., Y. Huang, C. Zhang, W. Wang, K. Tan, and R. Du (2015), Crustal deformation on the Chinese mainland during 19982014 based on GPS data, *Geodesy and Geodynamics*, *6*(1), 7–15, doi:10.1016/j.geog.2014.12.006.

Zheng, B., S. Guo, and H. Xu (1981), Preliminary study of principal features of the NW and NWW trending fault structures in the Yanshan region, *Seismology and Geology*, *3*(2), 31–40 (in Chinese).

Zheng, D., P. Z. Zhang, J. Wan, D. Yuan, C. Li, G. Yin, G. Zhang, Z. Wang, W. Min, and J. Chen (2006), Rapid exhumation at ˜ 8 Ma on the Liupan Shan thrust fault from apatite fission-track thermochronology: Implications for growth of the northeastern Tibetan Plateau margin, *Earth and Planetary Science Letters*, *248*(1-2), 183–193, doi:10.1016/j.epsl.2006.05.023.

Zhou, M., T. Lü, Y. Zhang, and A. Ruan (2000), The geological structure background and the crustal structure in the northeastern margin of the Qinghai-Tibetan plateau, *Acta Seismologica Sinica*, *13*(6), 687–697, doi:10.1007/s11589-000-0071-2.

Zhou, Y., B. Parsons, J. R. Elliott, I. Barisin, and R. T. Walker (2015), Assessing the ability of Pleiades stereo imagery to determine height changes in earthquakes: A case study for the El Mayor-Cucapah epicentral area, *Journal of Geophysical Research (Solid Earth)*, *120*, 8793–8808, doi:10.1002/2015JB012358.Received.

**Table 1.** Lateral offset measurements on the Luoshan Fault[a]

| Feature | Latitude / ° | Longitude / ° | Lateral offset / m |
|---|---|---|---|
| *Xiaoluoshan* | | | |
| Thalweg | 37.1840 | 106.3353 | 30.2 |
| Thalweg | 37.1826 | 106.3358 | 41.2 |
| Riser top | 37.1816 | 106.3361 | 29.2 |
| Riser top | 37.1811 | 106.3364 | 33.1 |
| Riser top | 37.1790 | 106.3374 | 40.2 |
| Riser bottom | 37.1789 | 106.3374 | 44.4 |
| Riser top | 37.1775 | 106.3379 | 35.2 |
| Riser top | 37.1766 | 106.3381 | 39.7 |
| Riser top | 37.1760 | 106.3384 | 42.0 |
| | | | 37.2±5.5[b] |
| *Tanzhuangzicun* | | | |
| Riser top | 37.4266 | 106.2793 | 57.0 |
| Riser bottom | 37.4263 | 106.2793 | 54.5 |
| Riser top | 37.4261 | 106.2793 | 61.4 |
| Riser top | 37.4232 | 106.2799 | 47.5 |
| Riser top | 37.4228 | 106.2799 | 48.0 |
| Riser top | 37.4173 | 106.2806 | 50.9 |
| Riser top | 37.4168 | 106.2806 | 45.8 |
| Thalweg | 37.4146 | 106.2810 | 50.1 |
| Riser top | 37.4120 | 106.2814 | 37.2 |
| Riser top | 37.4117 | 106.2814 | 54.0 |
| | | | 50.6±6.7[c] |
| *Shiyaodong* | | | |
| Thalweg | 37.2521 | 106.3201 | 33.8 |
| Thalweg | 37.2508 | 106.3203 | 48.5 |
| Thalweg | 37.2493 | 106.3205 | 44.5 |
| Thalweg | 37.2483 | 106.3204 | 41.9 |
| Thalweg | 37.2466 | 106.3201 | 36.9 |
| | | | 41.1±5.9[d] |

[a] Latitudes and longitudes are for the intersection of the western piercing line with the mapped fault trace.

[b] Mean offset and standard deviation for the Xiaoluoshan section.

[c] Mean offset and standard deviation for the Tanzhuangzicun section.

[d] Mean offset and standard deviation for the Shiyaodong section, re-measured after *Min et al.* [2003].

**Table 2.** IRSL dating results

| Location | Name | Lat | Long | Elevation | Depth | Equivalent Dose | Dose Rate | Age[a] |
|---|---|---|---|---|---|---|---|---|
| | | ° | ° | m | m | Gy | mGy $a^{-1}$ | ka |
| Xiaoluoshan Fault | 1 | 106.3350 | 37.1850 | 1761 | 2.1 | | | 141±12 |
| Xiaoluoshan Fault | 2 | 106.3397 | 37.1780 | 1766 | 0.55 | | | 9.16±0.57 |
| Daluoshan Fault | 3 | 106.2800 | 37.4250 | 1422 | 1.7 | | | 10.6±0.9 |
| East Helanshan Fault | 4 | 106.6575 | 39.2360 | 1374 | 0.54 | | | 1.27±0.14 |
| East Helanshan Fault | 5 | 106.6575 | 39.2360 | 1374 | 1.3 | | | 3.21±0.21 |

[a] Including $1\sigma$ analytical uncertainties.

**Table 3.** Calculated slip rates and throw rates

| Location | Sample No. | Latitude ° | Longitude ° | Age ka | Error ka | Horizontal Offset m | Error m | Slip rate mm/a | Error mm/a |
|---|---|---|---|---|---|---|---|---|---|
| *Luoshan Fault* | | | | | | | | | |
| Xiaoluoshan | IRSL 1 | 37.1850 | 106.3350 | 141 | 12 | 37.2 | 5.5 | 0.26 | 0.05 |
| Xiaoluoshan | IRSL 2 | 37.1780 | 106.3397 | 9.16 | 0.57 | 37.2 | 5.5 | 4.1 | 0.7 |
| Tanzhuangzicun | IRSL 3 | 37.4250 | 106.2800 | 10.6 | 0.9 | 50.6 | 6.7 | 4.8 | 0.8 |
| Shiyaodong[a] | TL | 37.2519 | 106.3204 | 9.80 | 0.75 | 41.1 | 5.9 | 4.2 | 0.7 |
| **Average**[b] | | | | | | | | **4.3** | **0.4**[c] |
| *East Helanshan Fault* | | | | | | | | | |
| Northern end of fault | IRSL 4 | 39.2360 | 106.6575 | 1.27 | 0.14 | 16.0 | 5.0 | 12.6 | 4.2 |
| Northern end of fault | IRSL 5 | 39.2360 | 106.6575 | 3.21 | 0.21 | 16.0 | 5.0 | 5.0 | 1.6 |

| Location | Sample No. | Latitude deg | Longitude deg | Age ka | Error ka | Vertical Offset m | Error m | Throw rate mm/a | Error mm/a |
|---|---|---|---|---|---|---|---|---|---|
| *East Helanshan Fault* | | | | | | | | | |
| Suyukou scarps, T5 | STM10[d] | 38.7839 | 106.1343 | 221.5 | 3.9 | 19.4 | 1.1 | 0.09 | 0.01 |
| Suyukou scarps, T5 | STM10[e] | 38.7839 | 106.1343 | 157.2 | 4.1 | 19.4 | 1.1 | 0.12 | 0.01 |
| Central Suyukou scarps | STM15[f] | 38.7063 | 106.0270 | 32.7 | 1.1 | 11.2 | 1.5 | 0.34 | 0.05 |
| Helanshan range-front | STM9 | 38.7359 | 106.0117 | 120.6 | 1.9 | 24.0 | 4.0 | 0.20 | 0.03 |
| Helanshan range-front | STM9[g] | 38.7359 | 106.0117 | 56.3 | 2.2 | 24.0 | 4.0 | 0.43 | 0.07 |
| **Sum**[h] | | | | | | | | **0.8** | **0.1** |
| **Extension rate**[i] | | | | | | | | **0.9** | **0.1** |

[a] Re-assessment of the data from Shiyaodong [*Min et al.*, 2003].

[b] Error-weighted average of samples IRSL 2, IRSL 3 and TL.

[c] Error is the weighted standard deviation of the three slip rate estimates.

[d] Assuming a zero inheritance model.

[e] Corrected for inheritance by subtracting STM13A.

[f] Corrected for inheritance by subtracting STM16C.

[g] Corrected for inheritance by subtracting STM13A.

[h] Sum of 0.34 and 0.43 mm/a for parallel Suyukou and range-front strands.

[i] Assuming the smallest fault dip found in the literature of 39 ° from *Fang et al.* [2009].

**Table 4.** $^{10}$Be dating results

| Location | Name | Type[a] | Lat<br>° | Long<br>° | Elevation<br>m | Thickness<br>cm | Density<br>g cm$^{-3}$ | Shielding<br>factor | [$^{10}$Be][b]<br>$10^3$ atoms g$^{-1}$ | Exposure<br>age[c] / ka |
|---|---|---|---|---|---|---|---|---|---|---|
| Range-front terrace | STM9 | A | 38.7359 | 106.0117 | 1461 | 2 | 2.65 | 0.9628 | 1498.0±22.7 | 120.6±1.9 |
| Range-front terrace | STM1 | B | 38.7363 | 106.0111 | 1486 | 3 | 2.70 | 0.9674 | 1409.0±24.7 | 111.5±2.0 |
| Range-front fan | STM3 | B | 38.7354 | 106.0143 | 1414 | 3 | 2.65 | 0.9832 | 206.2±7.0 | 16.5±0.6 |
| Range-front fan | STM4 | B | 38.7353 | 106.0138 | 1413 | 3 | 2.73 | 0.9832 | 163.5±11.4 | 13.1±0.9 |
| Range-front fan | STM5 | B | 38.7354 | 106.0138 | 1411 | 3 | 2.75 | 0.9832 | 101.9±13.3 | 8.2±1.1 |
| Range-front fan | STM6 | B | 38.7354 | 106.0138 | 1419 | 3 | 2.73 | 0.9832 | 138.7±6.5 | 11.1±0.5 |
| Range-front fan | STM7 | B | 38.7349 | 106.0149 | 1400 | 3 | 2.73 | 0.9795 | 219.0±6.7 | 17.8±0.6 |
| Range-front fan | STM8 | B | 38.7344 | 106.0150 | 1399 | 3 | 2.74 | 0.9795 | 469.0±16.4 | 38.3±1.4 |
| T5 | STM10 | A | 38.7839 | 106.1343 | 1193 | 2 | 2.67 | 0.9996 | 2288.0±38.3 | 221.5±3.9 |
| T5 | STM11A | C | 38.7828 | 106.1398 | 1162 | 4 | 2.65 | 0.9996 | 1560.6±32.5 | 154.4±3.3 |
| T5 | STM11B | C | 38.7828 | 106.1398 | 1162 | 4 | 2.65 | 0.9996 | 2161.5±29.8 | 217.0±3.2 |
| T5 | STM11C | C | 38.7828 | 106.1398 | 1162 | 4 | 2.65 | 0.9996 | 2094.9±23.4 | 209.6±2.5 |
| T5 | STM11D | C | 38.7828 | 106.1398 | 1162 | 4 | 2.65 | 0.9996 | 1084.5±17.0 | 105.6±1.7 |
| T5 | STM11E | C | 38.7828 | 106.1398 | 1162 | 4 | 2.65 | 0.9996 | 1820.7±43.3 | 181.3±4.5 |
| T5 | STM11F | C | 38.7828 | 106.1398 | 1162 | 4 | 2.65 | 0.9996 | 2215.7±23.4 | 223.4±2.5 |
| T5 | STM11G | C | 38.7828 | 106.1398 | 1162 | 4 | 2.65 | 0.9996 | 2134.5±36.8 | 213.9±3.9 |
| T5 | STM11H | C | 38.7828 | 106.1398 | 1162 | 4 | 2.65 | 0.9996 | 2054.8±46.8 | 205.4±4.9 |
| T5 (inheritance) | STM12 | A | 38.7766 | 106.1285 | 1194 | 2 | 2.67 | 0.9996 | 299.0±7.5 | 27.5±0.7 |
| T5 (inheritance) | STM13A | C | 38.7766 | 106.1285 | 1194 | 4 | 2.68 | 0.9996 | 679.6±12.2 | 64.3±1.2 |
| T5 (inheritance) | STM13B | C | 38.7766 | 106.1285 | 1194 | 4 | 2.68 | 0.9996 | 85.4±3.8 | 8.0±0.4 |
| T2 | STM14 | A | 38.7047 | 106.0248 | 1254 | 2 | 2.66 | 0.9993 | 209.9±5.5 | 18.5±0.5 |
| T2 | STM14A | C | 38.7047 | 106.0248 | 1254 | 4 | 2.66 | 0.9993 | 96.9±3.6 | 8.7±0.3 |
| T2 | STM14B | C | 38.7047 | 106.0248 | 1254 | 4 | 2.66 | 0.9993 | 859.5±16.2 | 78.0±1.5 |
| T2 | STM14C | C | 38.7047 | 106.0248 | 1254 | 4 | 2.66 | 0.9993 | 110.4±7.7 | 9.8±0.7 |
| T3 | STM15 | A | 38.7063 | 106.0270 | 1251 | 2 | 2.67 | 0.9993 | 475.7±11.5 | 42.3±1.0 |
| T2 & T3 (inheritance) | STM16 | A | 38.7080 | 106.0330 | 1264 | 2 | 2.69 | 0.9993 | 165.0±8.0 | 14.4±0.7 |
| T2 & T3 (inheritance) | STM16A | C | 38.7080 | 106.0330 | 1264 | 5 | 2.69 | 0.9993 | 108.3±3.3 | 9.7±0.3 |
| T2 & T3 (inheritance) | STM16B | C | 38.7080 | 106.0330 | 1264 | 5 | 2.69 | 0.9993 | 226.1±5.4 | 20.3±0.5 |
| T2 & T3 (inheritance) | STM16C | C | 38.7080 | 106.0330 | 1264 | 5 | 2.69 | 0.9993 | 107.4±3.7 | 9.6±0.3 |
| T2 & T3 (inheritance) | STM16D | C | 38.7080 | 106.0330 | 1264 | 5 | 2.69 | 0.9993 | 373.8±8.3 | 33.6±0.8 |

[a] A = aggregate of pebbles; B = boulder top; C = clast

[b] Background corrected values. Errors are analytical AMS uncertainties for samples and blanks propagated in quadrature. The NIST_ 27900 standard, with a ratio of 2.79 x $10^{-11}$ was used for all samples.

[c] Exposure ages were calculated with the CRONUS-Earth online calculator (version 2.2), using a constant production rate model and a sea-level high-latitude reference production rate of 4.49±0.39 atoms g$^{-1}$ yr$^{-1}$ [*Lal*, 1991; *Stone*, 2000; *Balco et al.*, 2008].

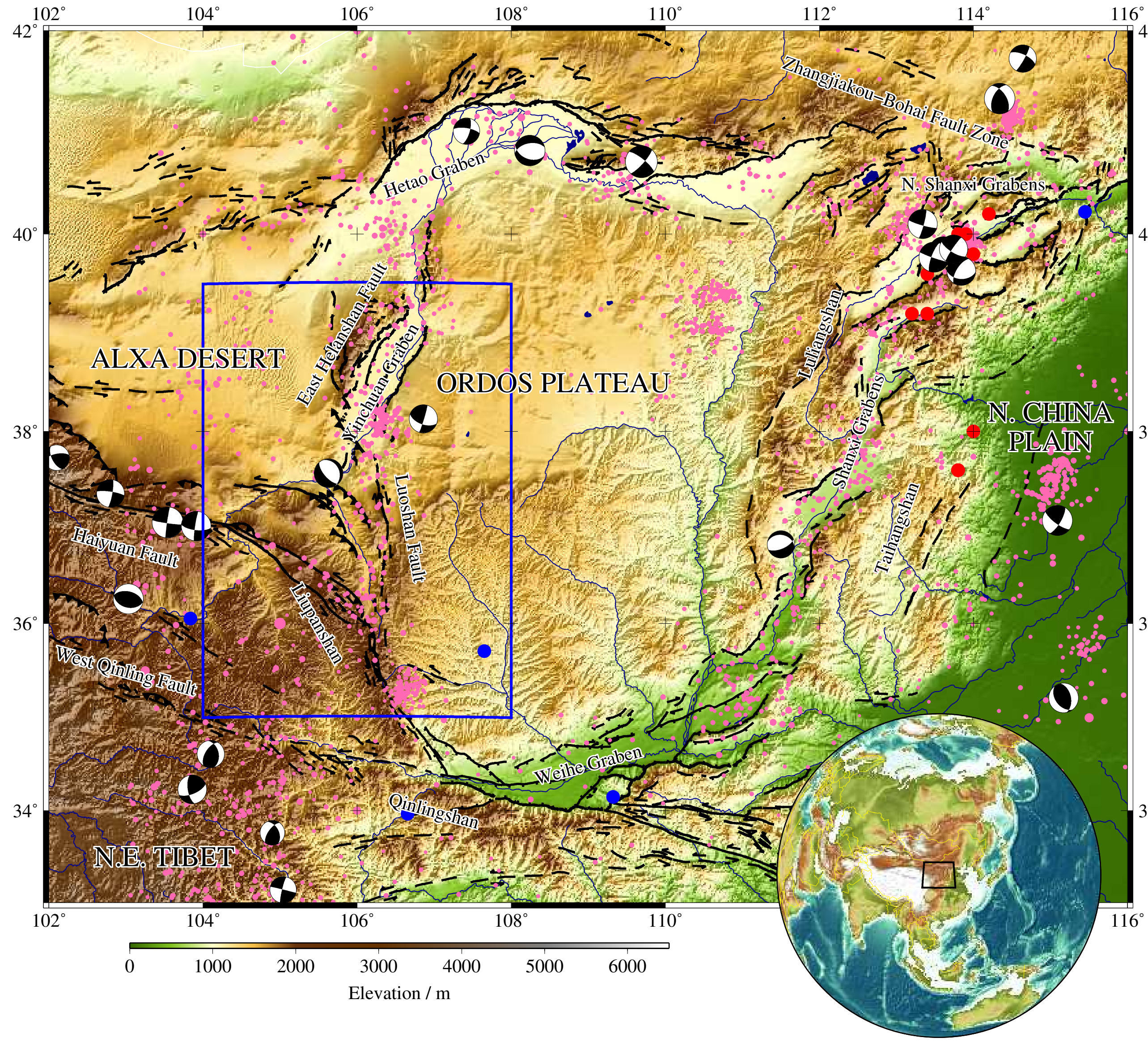
102°
104°
106°
108°
110°
112°
114°
116°
42°
40°
38°
36°
34°
Zhangjiakou–Bohai Fault Zone
Hetao Graben
N. Shanxi Grabens
ALXA DESERT
East Helanshan Fault
Yinchuan Graben
ORDOS PLATEAU
Lüliangshan
Shanxi Grabens
N. CHINA PLAIN
Luoshan Fault
Taihangshan
Haiyuan Fault
Liupanshan
West Qinling Fault
Weihe Graben
Qinlingshan
N.E. TIBET
0
1000
2000
3000
4000
5000
6000
Elevation / m

**Figure 1.** SRTM topography of the Ordos Plateau in northeastern China [*Farr et al.*, 2007]. Focal mechanisms from the Global CMT catalogue [*Ekström et al.*, 2012] are shown for recent earthquakes (1976 to present) with magnitudes greater than $M_w$ 5.0. Earthquakes of $M_w$ 2.0-5.0 since 1920 from the ISC catalogue [*International Seismological Centre*, 2013] are shown as pink dots. Faults, marked as thin black lines, have been mapped from satellite imagery (source: http://earth.google.com) based upon earlier fault maps from *Tapponnier and Molnar* [1977], *Deng et al.* [1984], *Zhang et al.* [1986], *Zhang et al.* [1990], *Xu and Ma* [1992], *Deng and Liao* [1996], *Darby and Ritts* [2002], *Yu* [2004] and *Darby et al.* [2005]. Faults that are inferred or show no clear evidence of Quaternary activity are marked by dashed lines. Red dots show locations of palaeomagnetism samples used by *Xu et al.* [1994]; blue dots show locations of palaeomagnetism samples used by *Li et al.* [2001]. Rivers are indicated in dark blue. The blue polygon indicates the region shown in Figure 3.

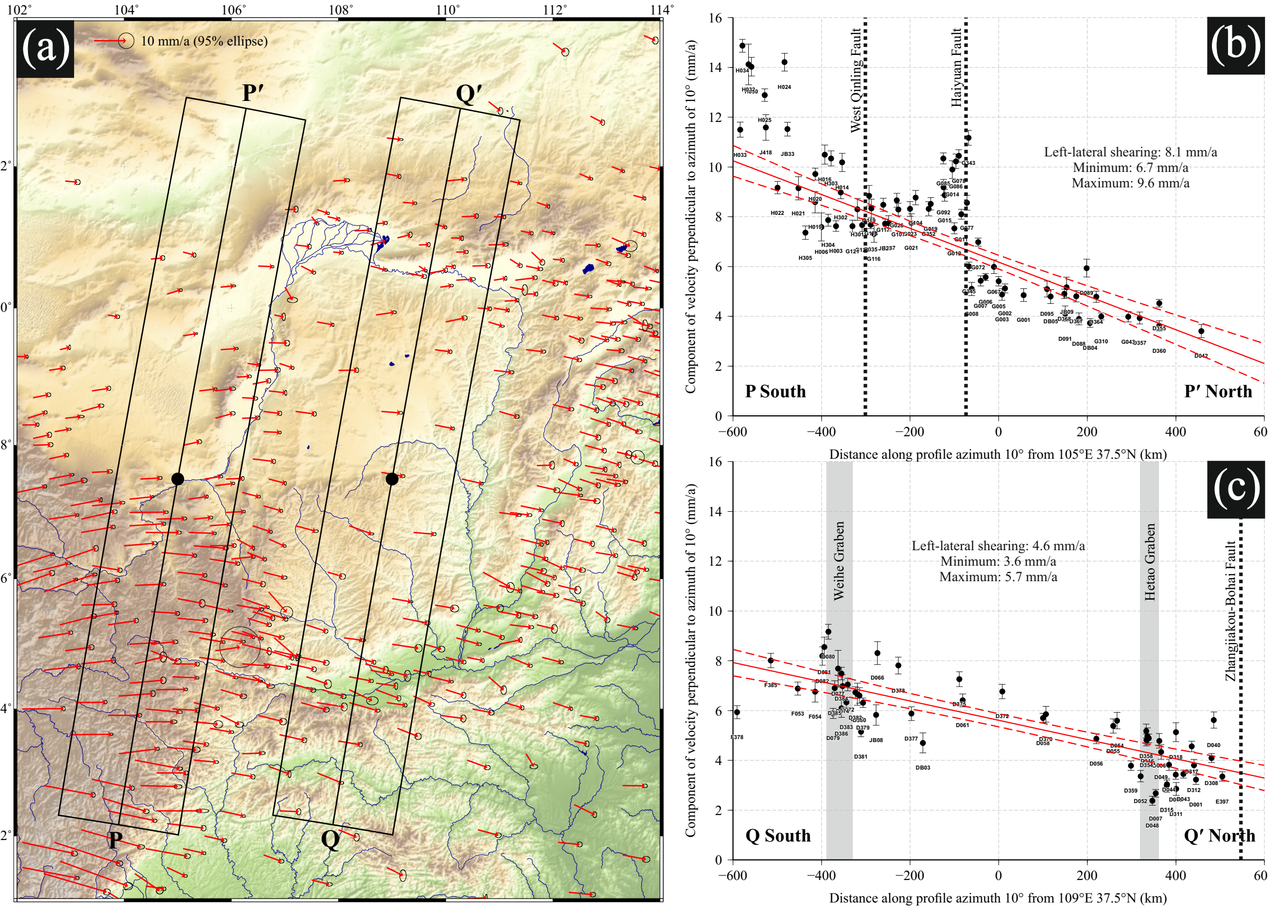
(a)
10 mm/a (95% ellipse)
102°
104°
106°
108°
110°
112°
114°
42°
40°
38°
36°
34°
32°
P
P′
Q
Q′
(b)
West Qinling Fault
Haiyuan Fault
Left-lateral shearing: 8.1 mm/a
Minimum: 6.7 mm/a
Maximum: 9.6 mm/a
P South
P′ North
Component of velocity perpendicular to azimuth of 10° (mm/a)
Distance along profile azimuth 10° from 105°E 37.5°N (km)
(c)
Weihe Graben
Hetao Graben
Zhangjiakou-Bohai Fault
Left-lateral shearing: 4.6 mm/a
Minimum: 3.6 mm/a
Maximum: 5.7 mm/a
Q South
Q′ North
Component of velocity perpendicular to azimuth of 10° (mm/a)
Distance along profile azimuth 10° from 109°E 37.5°N (km)
0
2
4
6
8
10
12
14
16
−600
−400
−200
0
200
400
600

**Figure 2.** (a) SRTM topography of the Ordos Plateau in northeastern China [*Farr et al.*, 2007]. Red arrows show campaign GPS measurements made over a period of 4 years (occupations in 2009, 2011 and 2013) from *Zhao et al.* [2015] relative to stable Eurasia. (b) Swath profile through the GPS data west of the Ordos Plateau showing the velocity component perpendicular to the profile. The red line is the best fit least squares regression to the data and the dashed red lines are the 95% confidence envelopes on this best fit line. The profile shows left-lateral shear of 8.1±1.5 mm/a averaged over the extent of the profile—with approximately 5 mm/a being taken up on the Haiyuan Fault. (c) Same as (b), but for a swath profile through the centre of the Ordos Plateau, showing left-lateral shear of 4.6±1.1 mm/a averaged over the extent of the profile—though it does not appear to be localised on any one individual structure. The difference between the two profiles is potentially due to absorption of some of the eastward motion in the Liupanshan thrust belt.

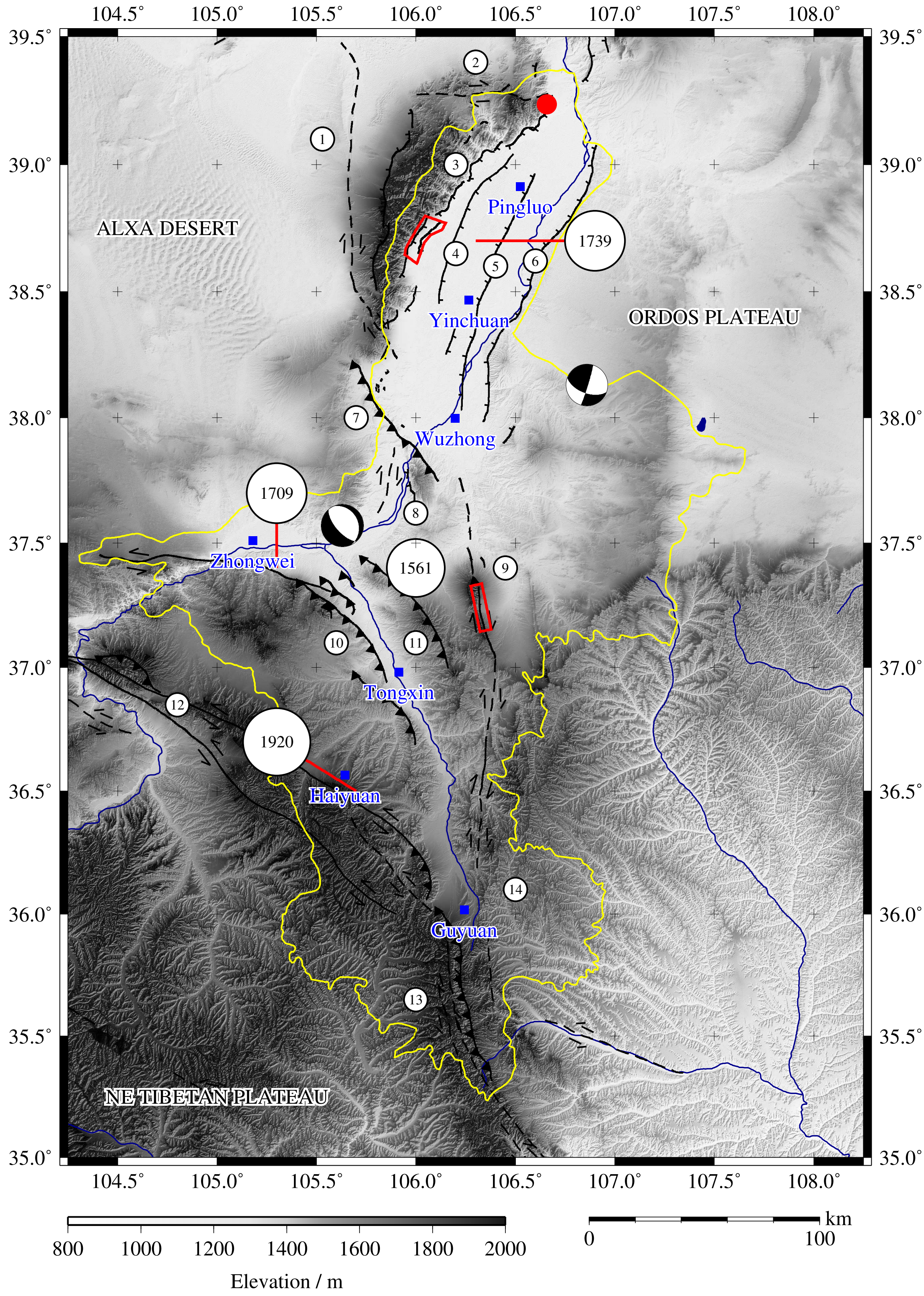
104.5°
105.0°
105.5°
106.0°
106.5°
107.0°
107.5°
108.0°
39.5°
39.0°
38.5°
38.0°
37.5°
37.0°
36.5°
36.0°
35.5°
35.0°
ALXA DESERT
ORDOS PLATEAU
NE TIBETAN PLATEAU
Pingluo
Yinchuan
Wuzhong
Zhongwei
Tongxin
Haiyuan
Guyuan
1739
1709
1561
1920
1
2
3
4
5
6
7
8
9
10
11
12
13
14
800
1000
1200
1400
1600
1800
2000
Elevation / m
0
100
km

**Figure 3.** SRTM topography (30 m resolution) of the study area in the western Ordos region, Ningxia Province, northern China [*Farr et al.*, 2007]. The province is outlined in yellow and cities are marked by blue squares. Focal mechanisms are from the Global CMT catalogue [*Ekström et al.*, 2012]. Major historical earthquakes are shown by white circles, including the year in which they occurred [*Liu et al.*, 2011]. Red outlines indicate coverage of Pleiades data. Red circle indicates field site at the northern end of the East Helanshan Fault (see Figure 15). Faults, marked as thin black lines, have been mapped from satellite imagery (source: http://earth.google.com) based upon earlier fault maps from *Tapponnier and Molnar* [1977], *Deng et al.* [1984], *Zhang et al.* [1990], *Darby and Ritts* [2002] and *Darby et al.* [2005]. Faults that are inferred or show no clear evidence of Quaternary activity are marked by dashed lines. Faults are numbered as follows (slip rates, where given are LL = left-lateral, RL = right-lateral and V = vertical): 1 Alxa Desert Fault; 2 Zhengyiguan Fault; 3 East Helanshan Fault, 0.5-0.8 mm/a V; 4 Luhuatai Fault; 5 Yinchuan-Pingluo Fault; 6 Yellow River (Huang He) Fault, 0.23-0.25 mm/a V; 7 Niushoushan Fault; 8 Baima Fault; 9 Luoshan Fault, 2.15±0.20 mm/a RL; 10 Tianjinshan-Miboshan (Zhongwei-Tongxin) Fault, 1.5-4.5 mm/a LL; 11 Yantongshan Fault; 12 Haiyuan Fault, 5-10 mm/a LL; 13 Liupanshan Fault; 14 Yunwushan Fault [*Zhang et al.*, 1990; *Min et al.*, 2000, 2003; *Deng et al.*, 2004; *Li et al.*, 2013]

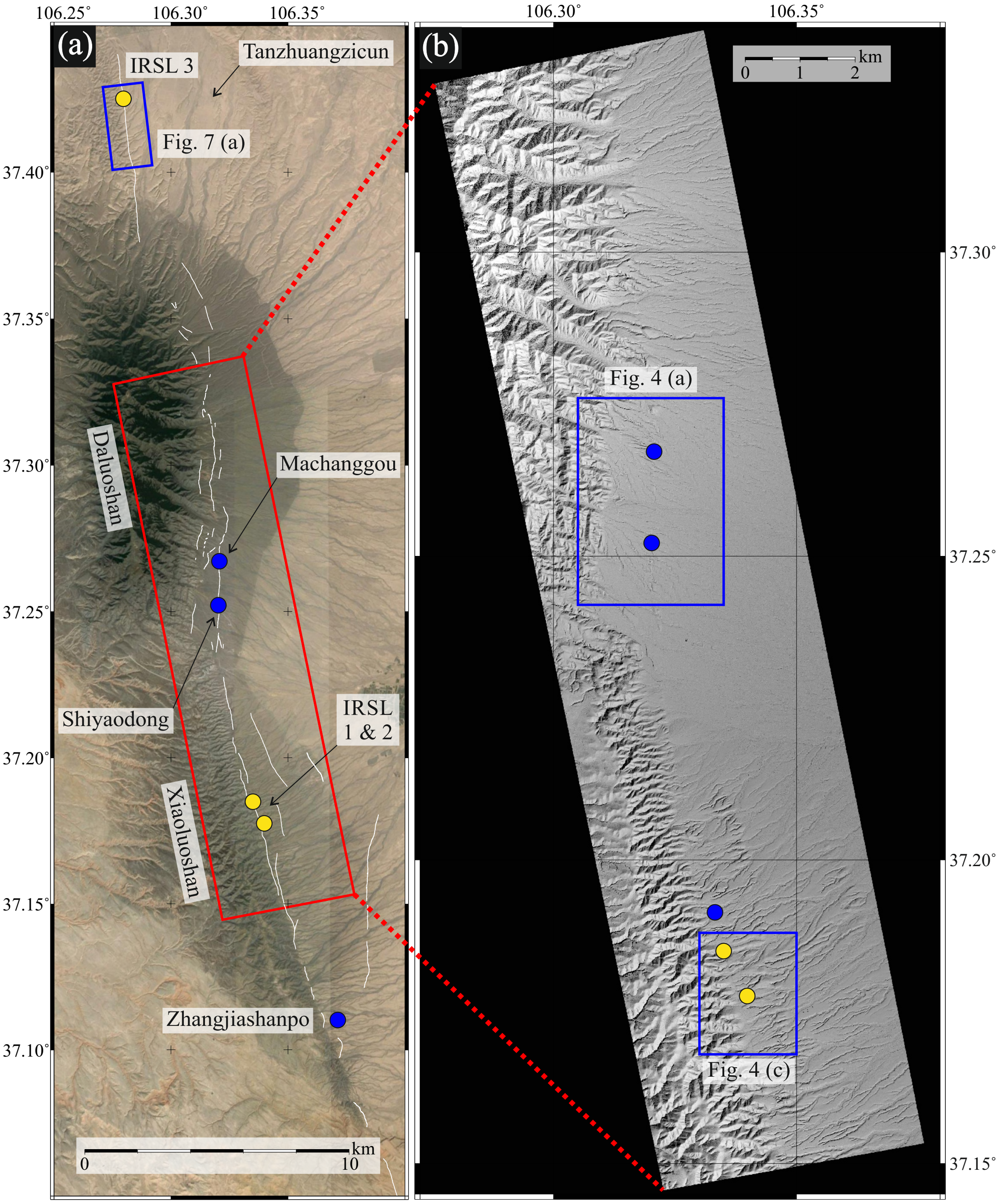

**Figure 4.** (a) Google Earth imagery from April and December 2013 (source: http://earth.google.com) of the Luoshan Fault with fault scarps mapped in white. Slip rate sites in this study are marked by yellow dots; sites from *Min et al.* [2003] are marked by blue dots. Red polygon shows coverage of Pleiades data. (b) Pleiades DEM of the central portion of the Luoshan Fault. Blue polygons show locations of other figures.

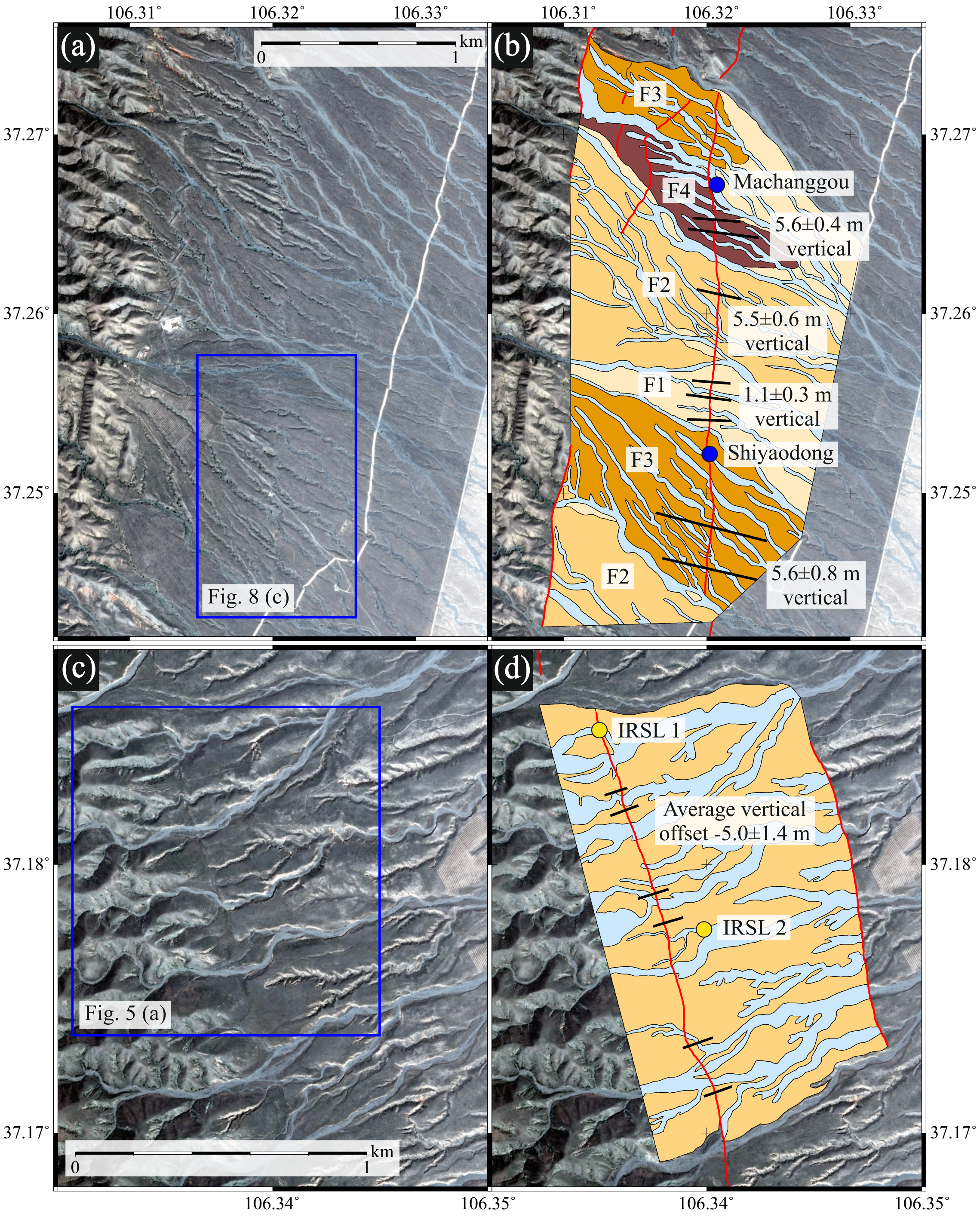
(a)
(b)
(c)
(d)
106.31°
106.32°
106.33°
37.27°
37.26°
37.25°
37.18°
37.17°
106.34°
106.35°
km
0
1
Fig. 8 (c)
Fig. 5 (a)
F1
F2
F3
F4
Machanggou
Shiyaodong
5.6±0.4 m vertical
5.5±0.6 m vertical
1.1±0.3 m vertical
5.6±0.8 m vertical
IRSL 1
IRSL 2
Average vertical offset -5.0±1.4 m

**Figure 5.** (a) Zoom of the Pleiades imagery in the vicinity of the slip rate sites used by *Min et al.* [2003]. (b) Annotated version of (a) with alluvial surfaces of different ages shown in different shades of brown and fault scarps mapped in red. Black lines indicate locations of topographic profiles used to estimate vertical offset preserved by each fan surface. (c) Zoom of the Pleiades imagery in the vicinity of the slip rate sites used in this study. Blue polygon shows location of Figure 6 (a). (d) Annotated version of (c). Black lines indicate locations of topographic profiles used to estimate average vertical offset preserved by this alluvial surface.

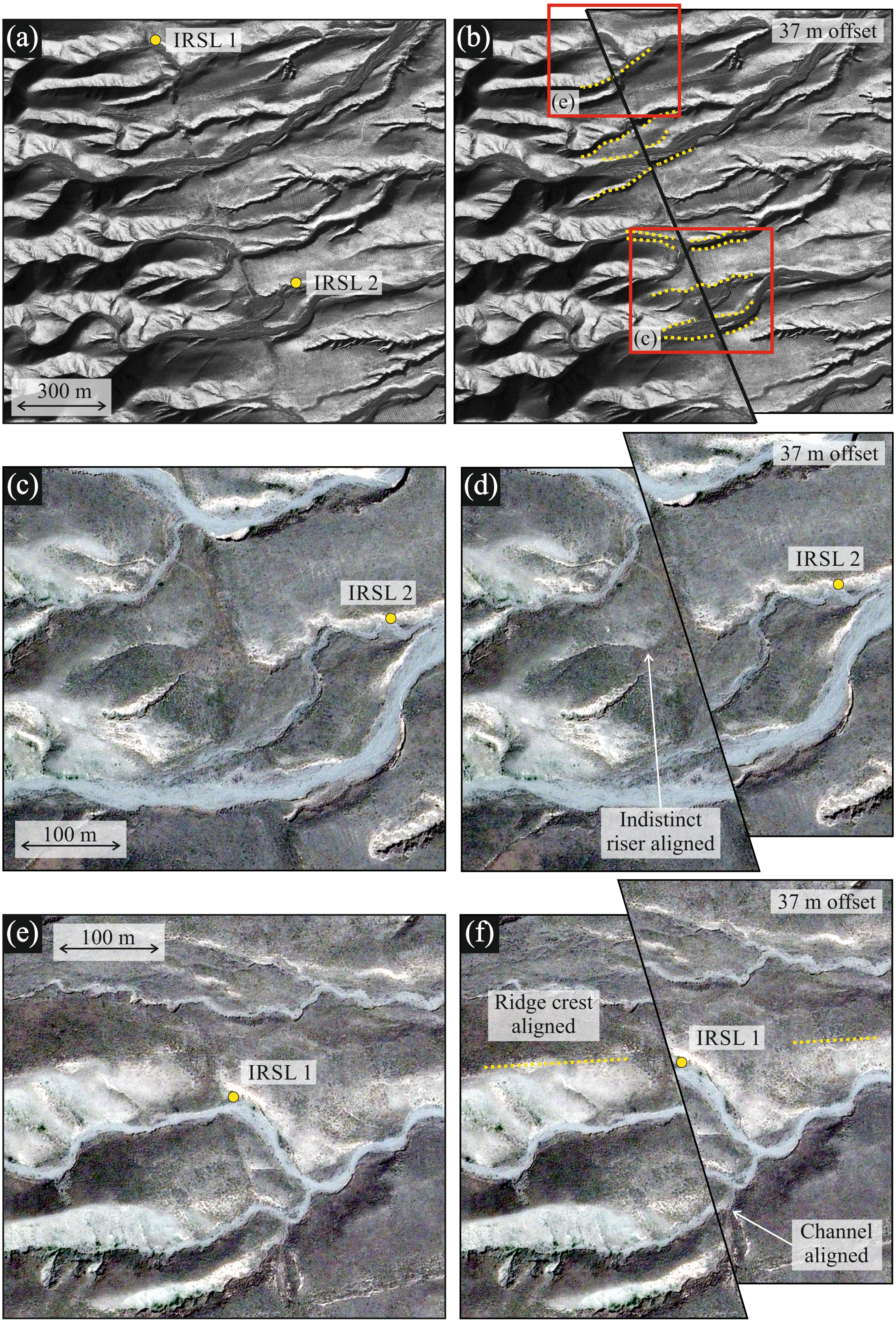
(a)
IRSL 1
IRSL 2
300 m
(b)
37 m offset
(e)
(c)
(c)
IRSL 2
100 m
(d)
37 m offset
IRSL 2
Indistinct riser aligned
(e)
100 m
IRSL 1
(f)
37 m offset
Ridge crest aligned
IRSL 1
Channel aligned

**Figure 6.** (a) 0.5 m resolution Worldview imagery showing a section of the Luoshan Fault adjacent to the Xiaoluoshan (see Figure 5 for precise location). The fault cuts across the image from north-northwest to south-southeast. The locations of IRSL samples 1 and 2 are indicated by yellow circles. (b) 37 m restoration, aligning various channel thalwegs and terrace risers (highlighted in yellow). Red boxes indicate locations of figures below. (c) 0.5 m resolution Pleiades imagery of the region marked in (b) and showing the location of IRSL sample 2. (d) Same as (c) with a 37 m restoration, aligning the sampled terrace riser. (e) 0.5 m resolution Pleiades imagery of the region marked in (b) and showing the location of IRSL sample 1. (d) Same as (e) with a 37 m restoration, aligning the channel thalweg to the south of the image and the ridge crest adjacent to the sampling site.

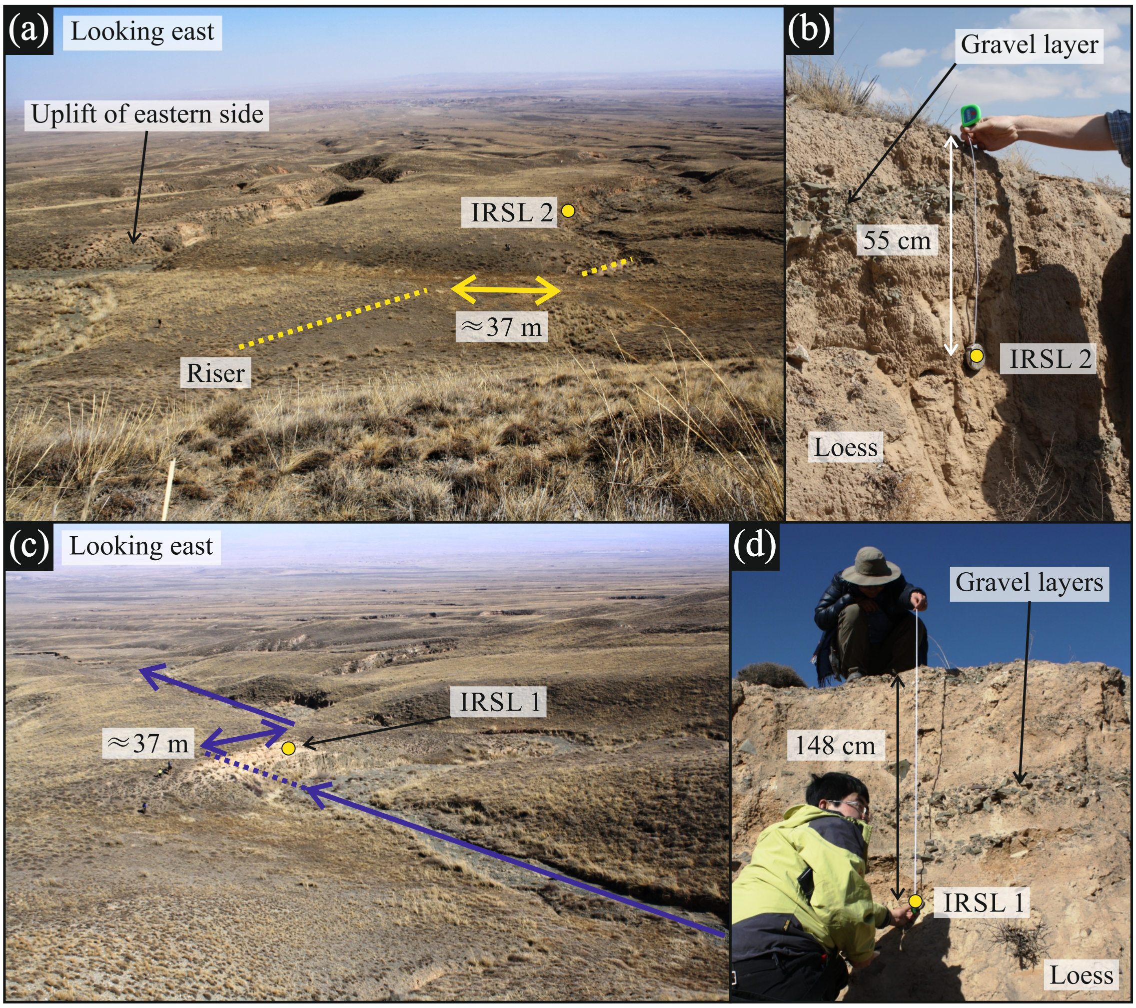

**Figure 7.** (a) Field photograph (taken at 37.178 °N, 106.340 °E) showing an overview of IRSL sample site 2. A riser on the western side of the fault trace, highlighted in yellow, can be identified by a change in the grass-cover. (b) Close-up field photograph showing the sedimentary context of IRSL sample 2. (c) Field photograph (taken at 37.185 °N, 106.335 °E) showing an overview of IRSL sample site 1. There is a large meander in the stream at the location of the fault trace, but the far-field offset is of the order of 37 m. (d) Close-up field photograph showing the sedimentary context of IRSL sample 1.

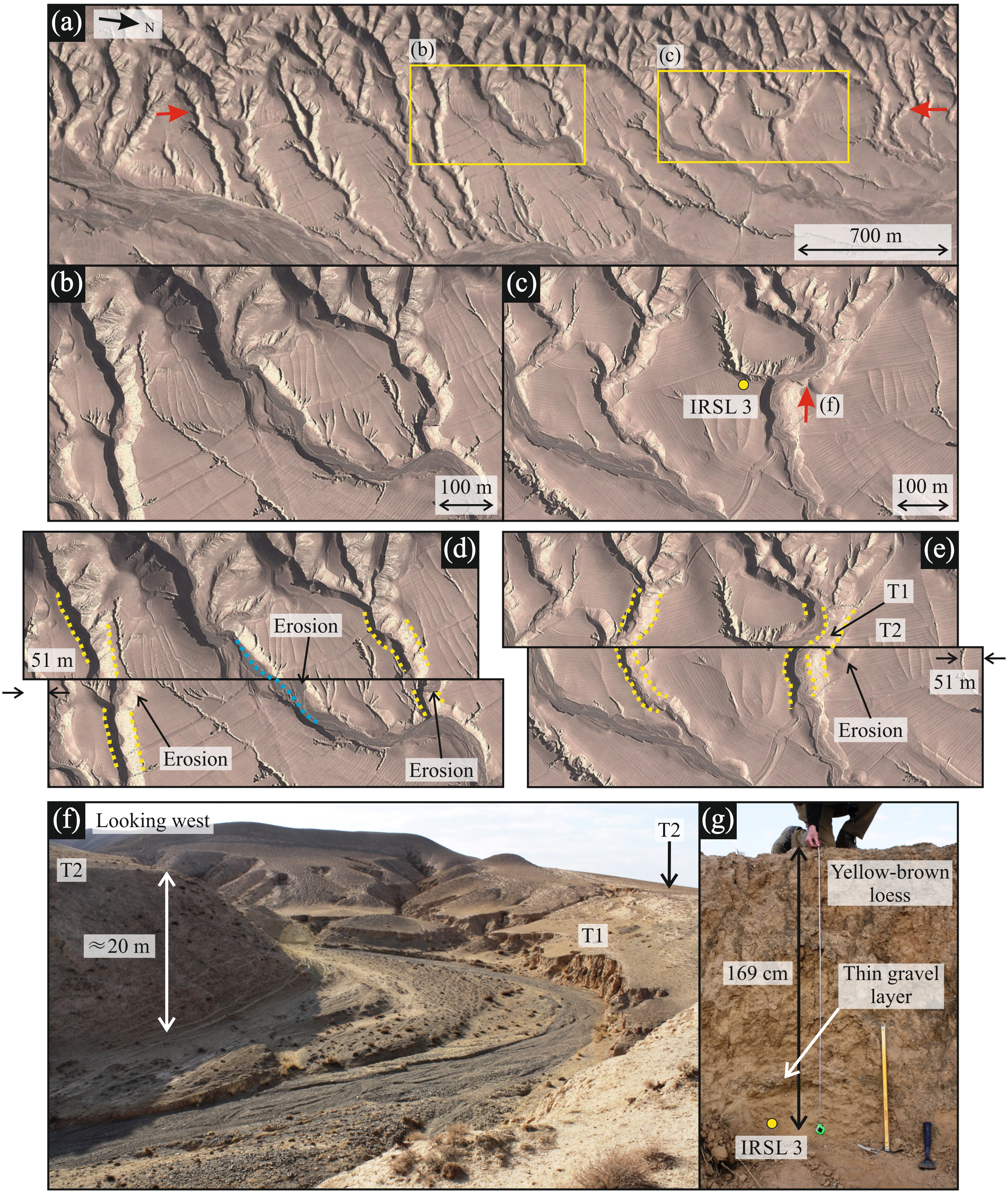
(a)
N
(b)
(c)
700 m
(b)
100 m
(c)
IRSL 3
(f)
100 m
(d)
Erosion
51 m
Erosion
Erosion
(e)
T1
T2
51 m
Erosion
(f)
Looking west
T2
T2
≈20 m
T1
(g)
Yellow-brown loess
169 cm
Thin gravel layer
IRSL 3

**Figure 8.** (a) Google Earth imagery from December 2013 (source: http://earth.google.com) of the Luoshan Fault north of the Daluoshan and around 1.75 km west of the village of Tanzhuangzicun (see Figure 4 (a) for precise location). Fault location is marked by red arrows. (b) Zoomed in view of the Google Earth imagery at the location marked in (a). (c) Zoomed in view of the Google Earth imagery at the location marked in (a). The location of IRSL sample 3 (at 37.425 °N, 106.280 °E) is indicated by the yellow circle. (d) Restoration of (b) indicating 51 m of right-lateral offset. Aligned channel risers are highlighted in yellow and an aligned channel thalweg is shown in blue. Eroded corners of channel margins on down-slope (i.e. northern) side are also indicated. (e) Restoration of (c) indicating 51 m of right-lateral offset. Yellow lines highlight alignment of two channel risers. (f) Field photograph (taken at the location indicated in (c) showing the two terrace levels adjacent to this channel. (g) Field photograph showing the sedimentary context of IRSL sample 3.

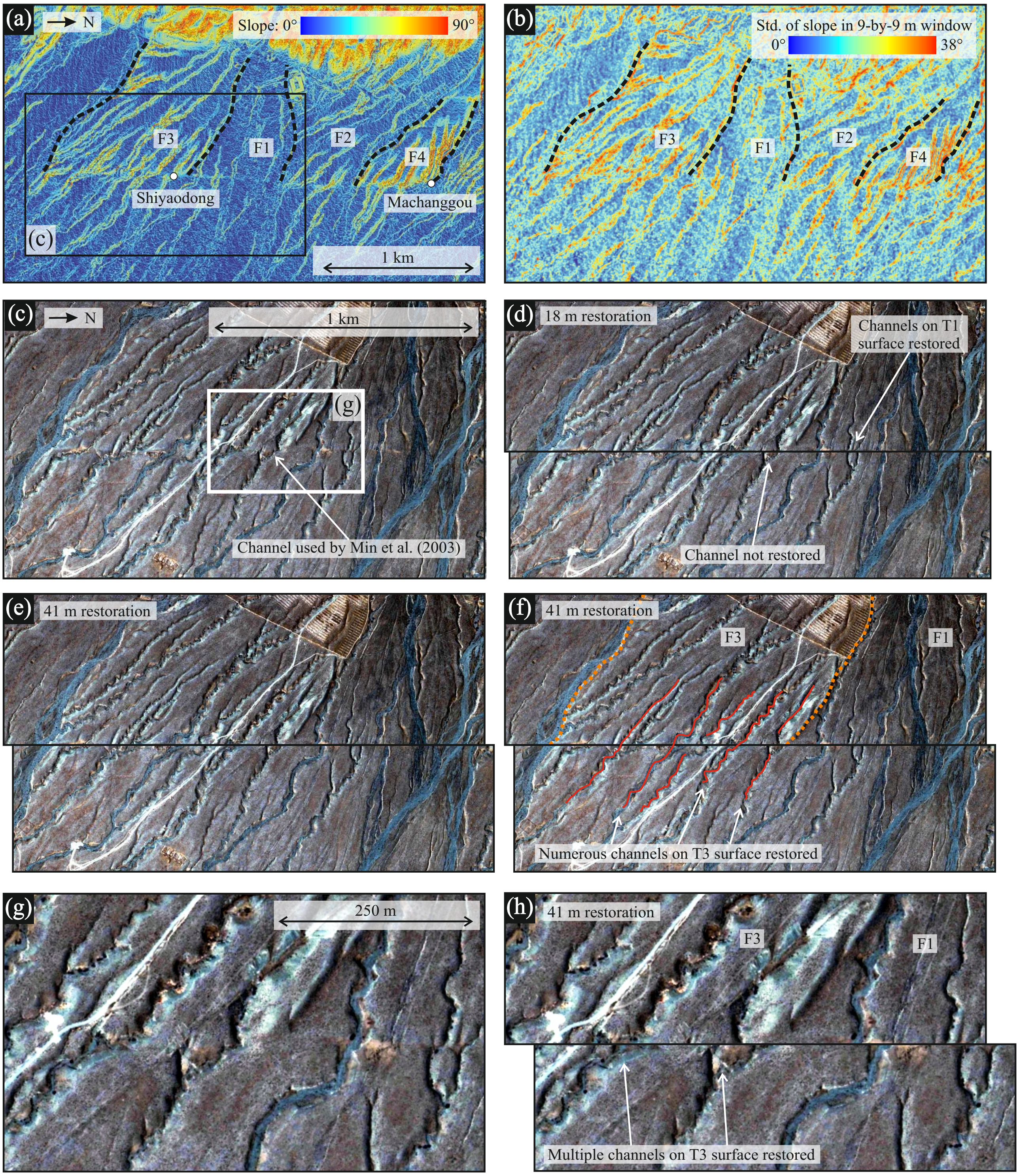
(a)
N
Slope: 0°
90°
F3
F1
F2
F4
Shiyaodong
Machanggou
(c)
1 km
(b)
Std. of slope in 9-by-9 m window
0°
38°
F3
F1
F2
F4
(c)
N
1 km
(g)
Channel used by Min et al. (2003)
(d)
18 m restoration
Channels on T1 surface restored
Channel not restored
(e)
41 m restoration
(f)
41 m restoration
F3
F1
Numerous channels on T3 surface restored
(g)
250 m
(h)
41 m restoration
F3
F1
Multiple channels on T3 surface restored

**Figure 9.** (a) Slope map derived from the Pleiades DEM. Region covered is the same as in Figure 5 (a). White dots show location of slip rate sites used by *Min et al.* [2003]. (b) Surface roughness map of the same area derived from the Pleiades DEM by taking the standard deviation of the slope of the DEM in a 9×9 m moving window [*Frankel and Dolan*, 2007]. (c) Pleiades imagery of the Shiyaodong site from *Min et al.* [2003] indicating the gully used for their slip rate estimate. (d) 18 m reconstruction, showing that gullies on the F1 surface are restored, but not those on the F3 surface. (e) 41 m reconstruction, which properly aligns gullies on the F3 surface. (f) Annotated version of (e) showing that multiple channels on the F3 surface can be restored with 41 m of right-lateral slip. (g) Zoomed in view of the gullies on the F3 and F1 surfaces at the location marked in (c). (h) Zoomed in view of the 41 m restoration.

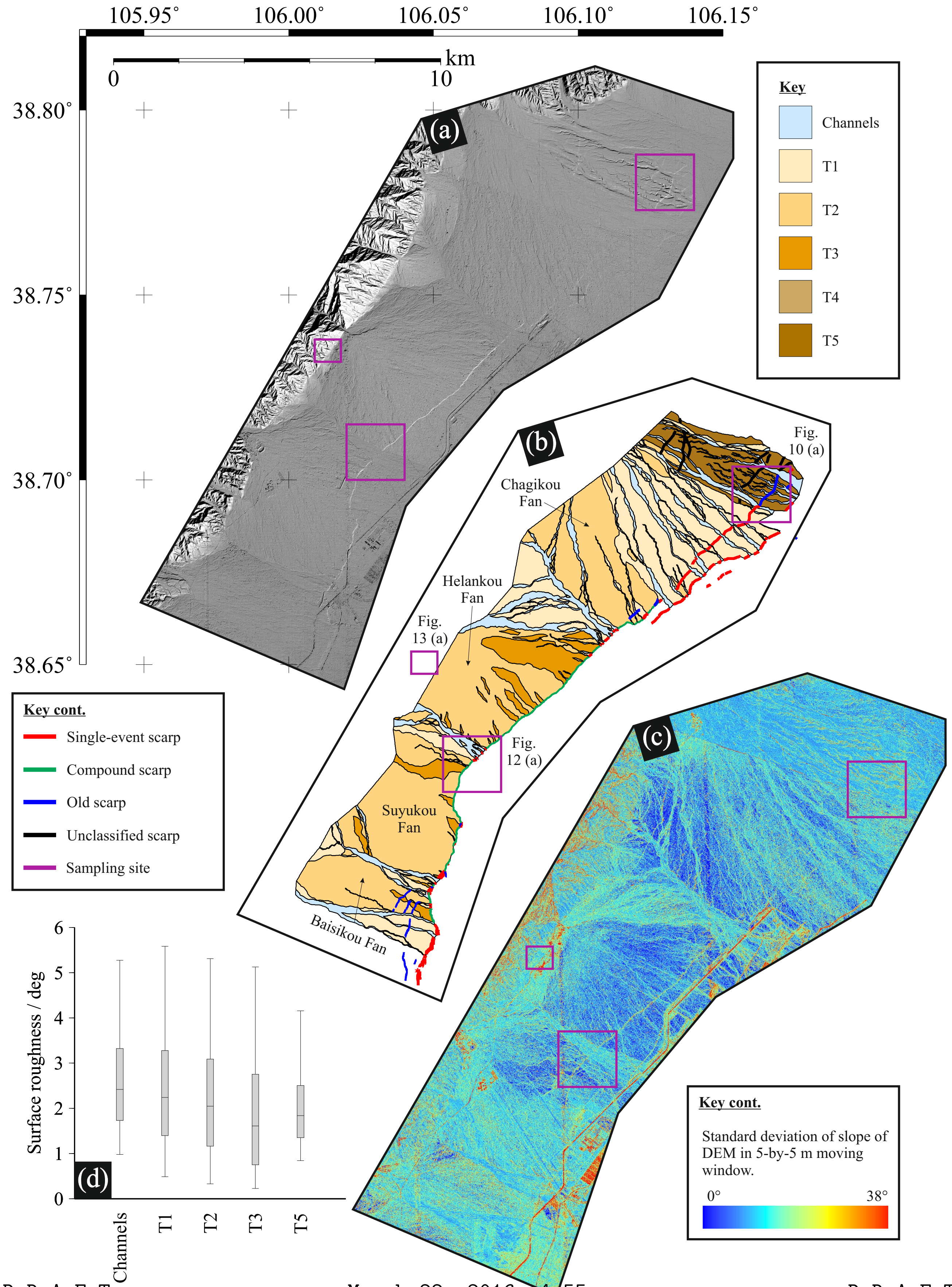
105.95°
106.00°
106.05°
106.10°
106.15°
38.80°
38.75°
38.70°
38.65°
0
10
km
(a)
(b)
(c)
(d)
Key
Channels
T1
T2
T3
T4
T5
Fig. 10 (a)
Chagikou Fan
Helankou Fan
Fig. 13 (a)
Fig. 12 (a)
Suyukou Fan
Baisikou Fan
Key cont.
Single-event scarp
Compound scarp
Old scarp
Unclassified scarp
Sampling site
Key cont.
Standard deviation of slope of DEM in 5-by-5 m moving window.
0°
38°
Surface roughness / deg
0
1
2
3
4
5
6
Channels
T1
T2
T3
T5

**Figure 10.** (a) Pleiades DEM for the Suyukou scarps at the southern end of the East Helanshan Fault. (b) Interpreted tectonic geomorphology for the Suyukou scarps at the southern end of the East Helanshan Fault. Purple polygons indicate the locations of $^{10}$Be sampling sites, as shown in Figure 13. (c) Surface roughness map derived from the Pleiades DEM by taking the standard deviation of the slope of the DEM in a 5×5 m moving window [*Frankel and Dolan*, 2007]. (d) Box-and-whisker plot of the surface roughness for each alluvial unit. The horizontal bar inside each box is the median roughness; the ends of the boxes are the 25th and 75th percentiles; and the whiskers indicate the 5th and 95th percentiles.

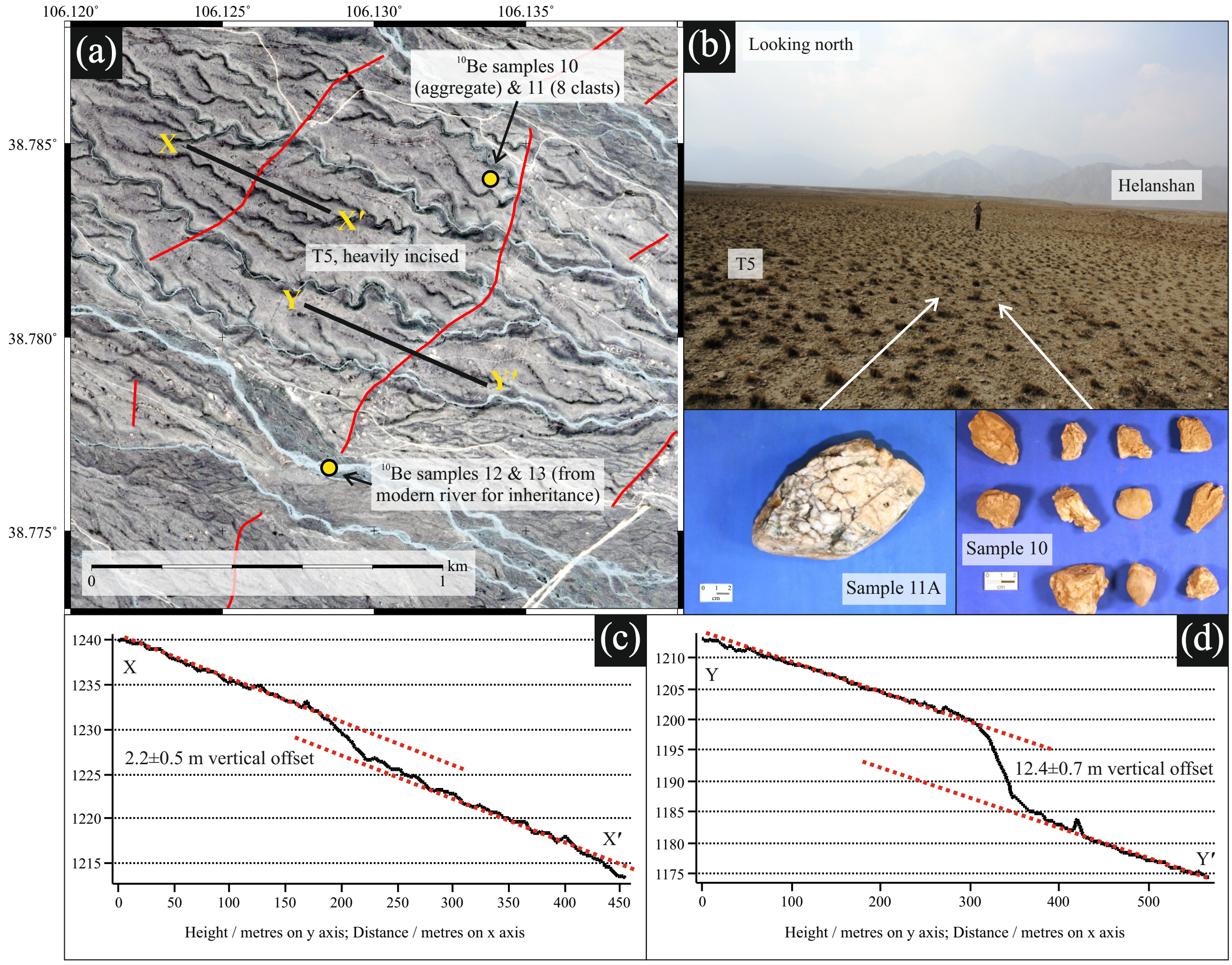

**Figure 11.** (a) Pleiades imagery showing the heavily incised T5 alluvial surface at the northern end of the Suyukou scarps. Fault traces are marked in red and $^{10}$Be sample locations are shown by yellow circles. (b) Field photograph (taken at 38.784 °N, 106.134 °E) of the T5 surface. Inset photographs show quartz pebbles collected from this surface for $^{10}$Be dating. (c) Topographic profile along the line X-X′ in (a), showing the vertical offset on one fault strand. (d) Topographic profile along the line Y-Y′ in (a), showing the vertical offset on another fault strand. Note that two other minor fault strands also offset T5 further to the northwest, giving a combined offset of 19.4±1.1 m.

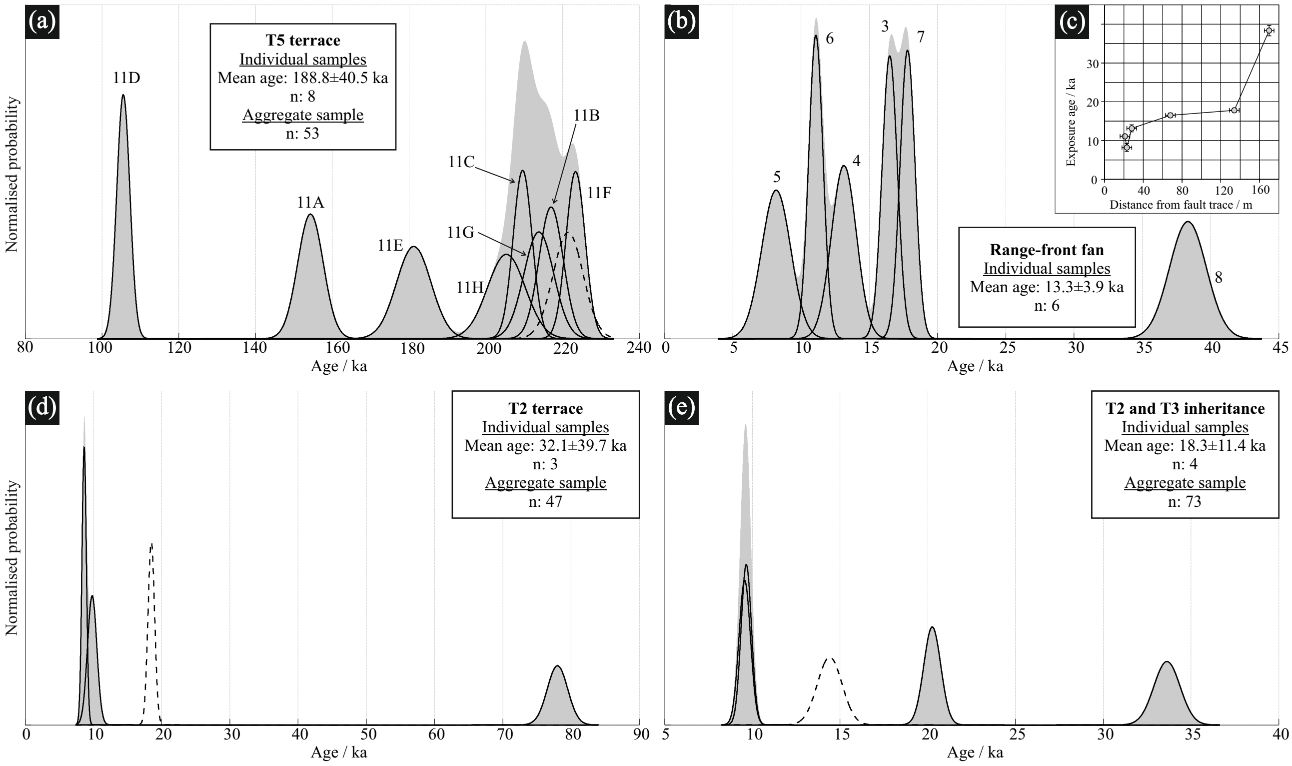

**Figure 12.** $^{10}$Be age results for (a) T5, (b) the range-front fan, (d) T2, and (e) the T2 and T3 inheritance. Black curves are normally distributed probability density functions (PDFs) for individual samples, defined by the age and the 1$\sigma$ analytical error. Grey curves are normal kernel density estimates (or camel plots), obtained by summing the individual PDFs. Dashed black curves are normally distributed PDFs for aggregate samples. (c) Plot of $^{10}$Be exposure age for boulder top samples from the range-front fan against their distance from the fault trace. Error bars show 1$\sigma$ analytical error on age measurements and an assumed error of ±5 m on the distance measurements.

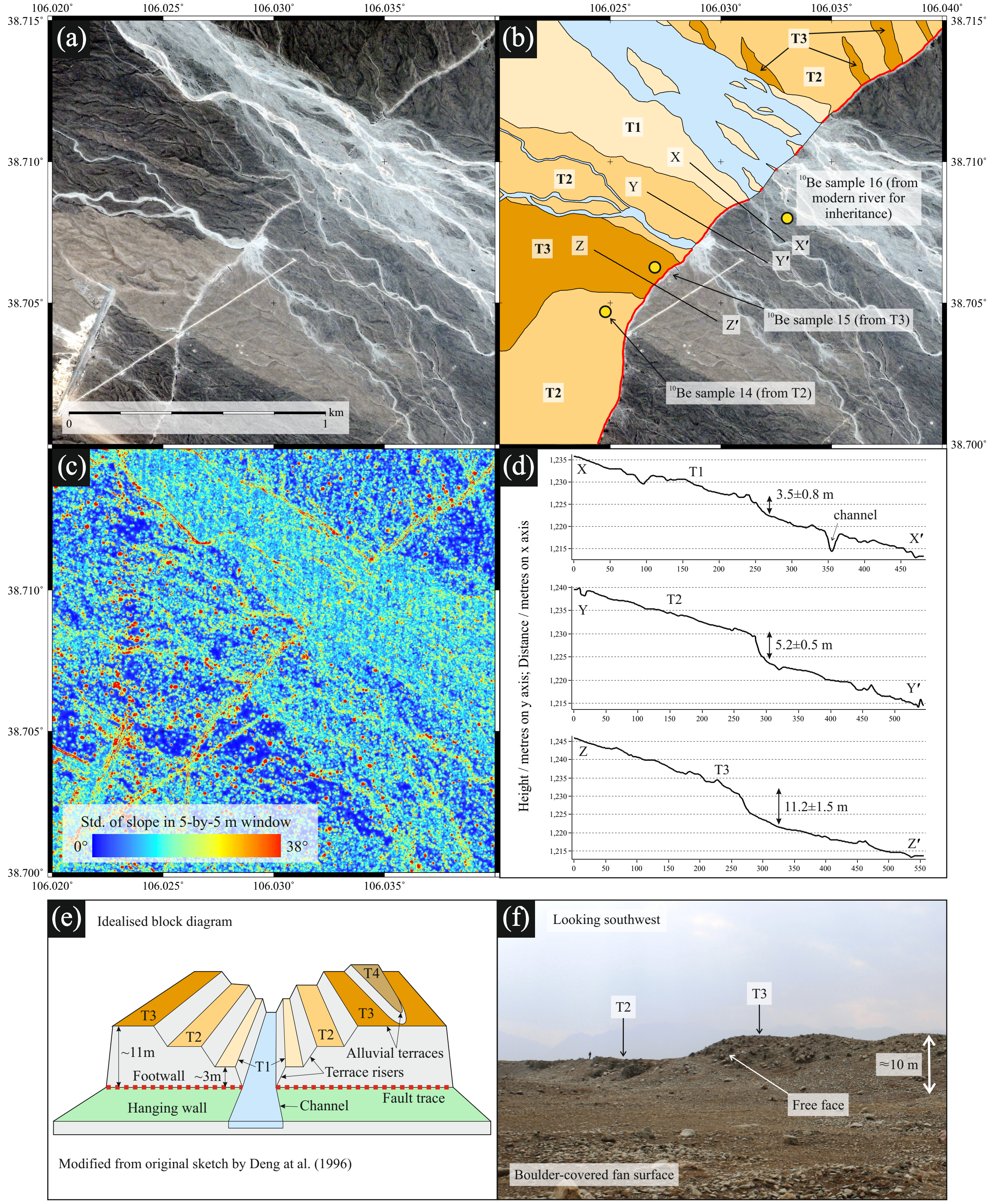
(a)
106.020°
106.025°
106.030°
106.035°
38.715°
38.710°
38.705°
0
1
km
(b)
106.040°
38.700°
T1
T2
T3
X
Y
Z
X′
Y′
Z′
$^{10}$Be sample 16 (from modern river for inheritance)
$^{10}$Be sample 15 (from T3)
$^{10}$Be sample 14 (from T2)
(c)
Std. of slope in 5-by-5 m window
0°
38°
(d)
Height / metres on y axis; Distance / metres on x axis
3.5±0.8 m
channel
5.2±0.5 m
11.2±1.5 m
(e)
Idealised block diagram
T4
~11m
Footwall
~3m
Alluvial terraces
Terrace risers
Hanging wall
Channel
Fault trace
Modified from original sketch by Deng at al. (1996)
(f)
Looking southwest
≈10 m
Free face
Boulder-covered fan surface

**Figure 13.** (a) Pleiades imagery showing an anastomosing river channel crossing the Suyukou scarps. (b) Annotated version of (a) showing mapped alluvial terrace surfaces, fault trace (in red), and $^{10}$Be sample locations (yellow circles). The locations of profiles X-X′, Y-Y′, and Z-Z′ are also indicated. (c) Surface roughness map derived from the Pleiades DEM by taking the standard deviation of the slope of the DEM in a 5×5 m moving window [*Frankel and Dolan*, 2007]. A number of the terraces mapped in (b) are visible in this image. (d) Three topographic profiles along the lines X-X′, Y-Y′, and Z-Z′ at the locations shown in (b). The three profiles show typical scarp heights for representative T1, T2, and T3 alluvial terrace surfaces. (e) Idealised block diagram showing the expected preservation of aggradational alluvial terraces in the footwall of a normal fault over multiple earthquake cycles. Modified from *Deng and Liao* [1996]. (f) Field photograph (taken at 38.706 °N, 106.028 °E) of the Suyukou scarps showing T2 and T3.

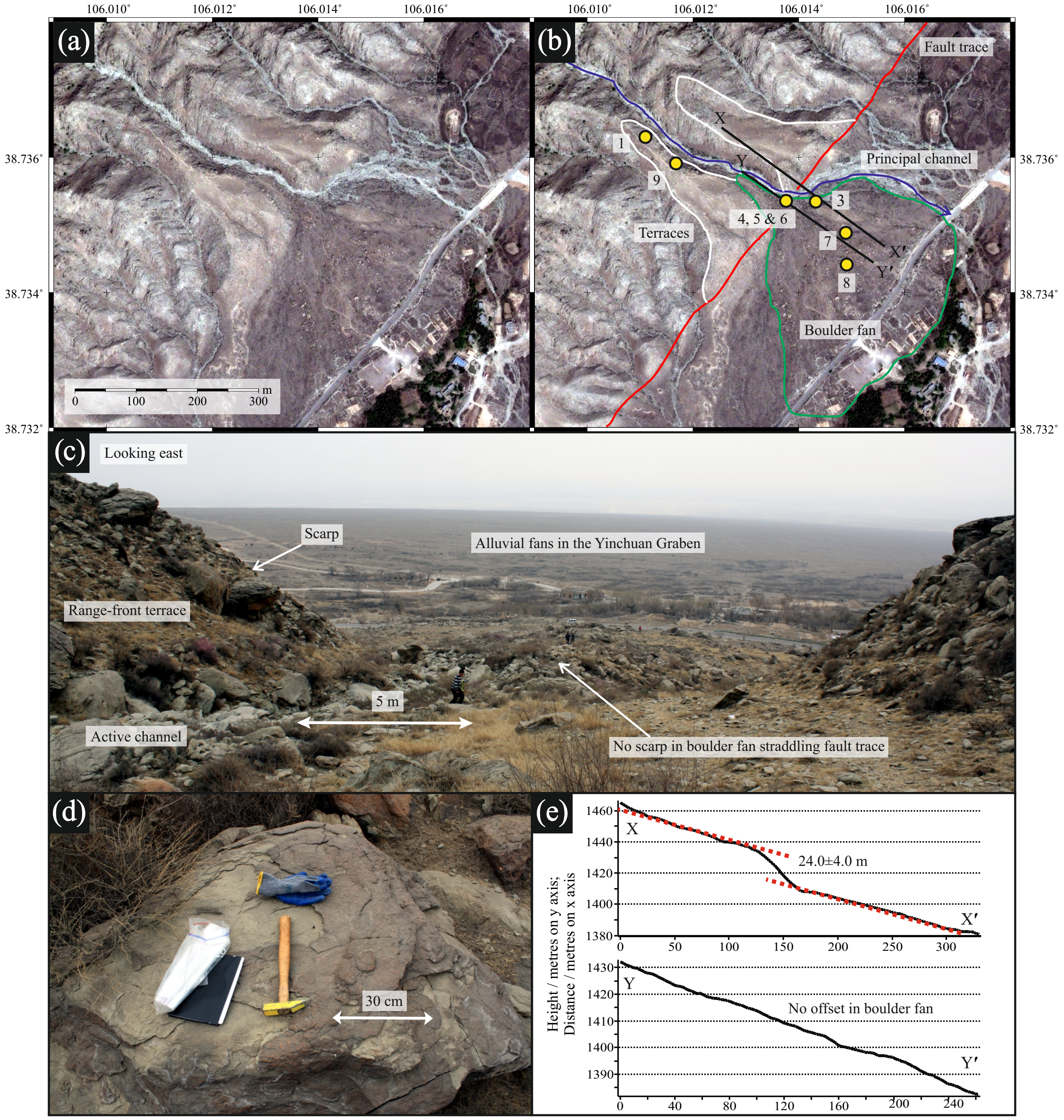
(a)
(b)
106.010°
106.012°
106.014°
106.016°
38.736°
38.734°
38.732°
0
100
200
300
m
Fault trace
Principal channel
Terraces
Boulder fan
X
X′
Y
Y′
1
3
4, 5 & 6
7
8
9
(c)
Looking east
Scarp
Alluvial fans in the Yinchuan Graben
Range-front terrace
5 m
Active channel
No scarp in boulder fan straddling fault trace
(d)
30 cm
(e)
Height / metres on y axis;
Distance / metres on x axis
24.0±4.0 m
No offset in boulder fan
1460
1440
1420
1400
1380
0
50
100
150
200
250
300
1430
1420
1410
1400
1390
0
40
80
120
160
200
240

**Figure 14.** (a) Pleiades imagery of the range-front fault on the eastern flank of the Helanshan. (b) Annotated version of (a) showing fault trace (in red), two uplifted footwall terraces (in white), and an alluvial fan that has been deposited on top of the fault (in green). Yellow circles mark locations where boulder tops were collected for $^{10}$Be exposure dating. (c) Annotated field photograph (taken at 38.735 °N, 106.014 °E) looking from the footwall, across the range-front fault trace, towards the boulder fan in the hanging wall. (d) Field photograph (taken at 38.735 °N, 106.014 °E) showing desert varnish on the top of the boulder where sample 4 was collected. (e) Topographic profiles from the Pleiades DEM along the lines marked X-X′ and Y-Y′ in (b).

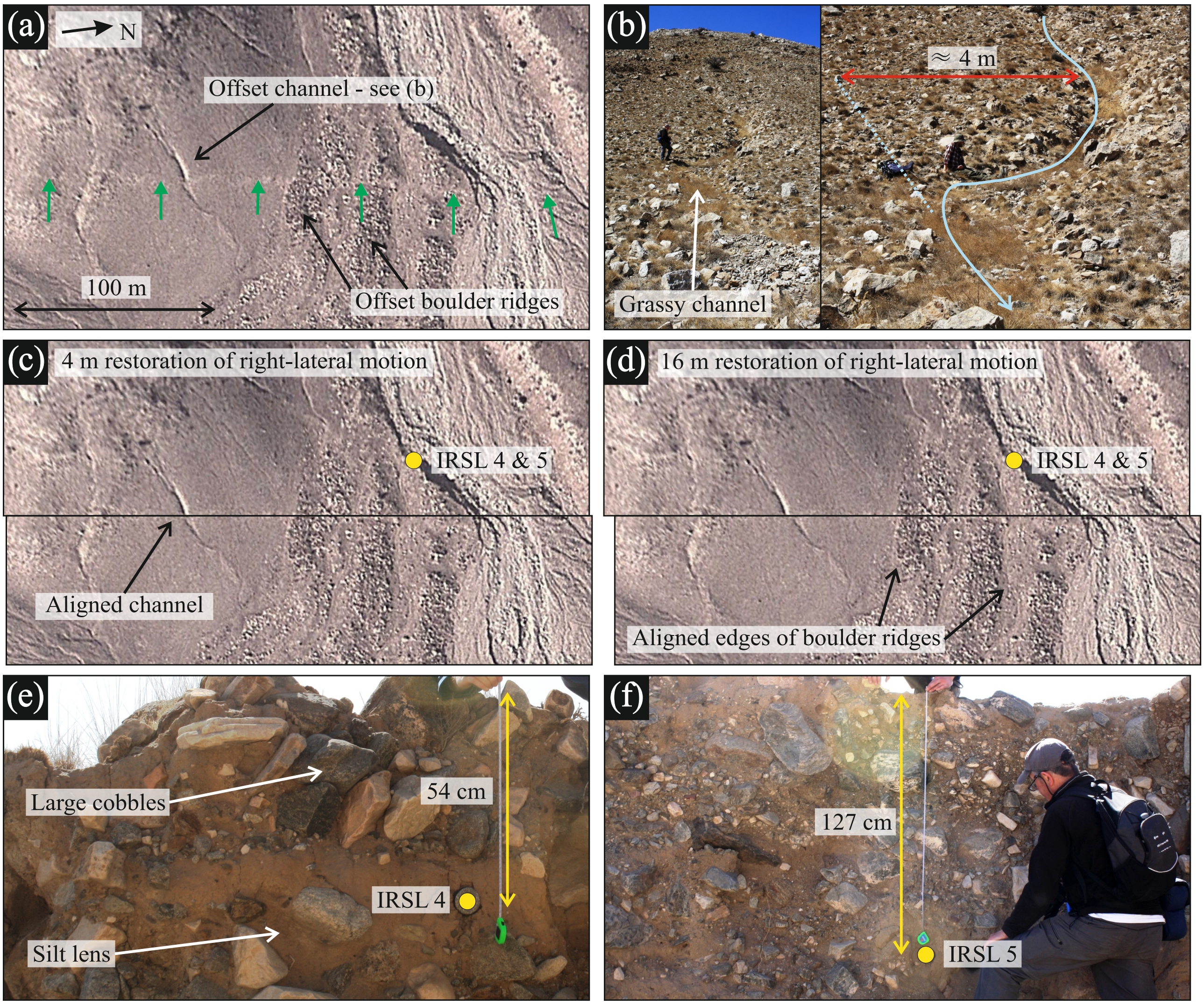

**Figure 15.** (a) Google Earth imagery from November 2011 (source: http://earth.google.com) of the northern end of the East Helanshan Fault, 10 km west of Huinong city. Fault scarp marked by green arrows and small offset visible in edges of boulder ridges. (b) Field photographs (taken at 39.235 °N, 106.658 °E, at the location marked in (a)). People for scale. The grassy channel records a right-lateral offset of approximately 4 m. (c) Same as (a) with a 4 m restoration of the right-lateral motion, which aligns the small channel shown in (b). Yellow circle indicates the location of IRSL samples 4 and 5. (d) Same as (a) with a 16 m restoration of the right-lateral motion, which aligns the edges of the boulder ridges as shown. Yellow circle indicates the location of IRSL samples 4 and 5. (e) Field photograph (taken at 39.236 °N, 106.658 °E) showing the sedimentary context of IRSL sample 4. (f) Field photograph (from the same location) showing the sedimentary context of IRSL sample 5.

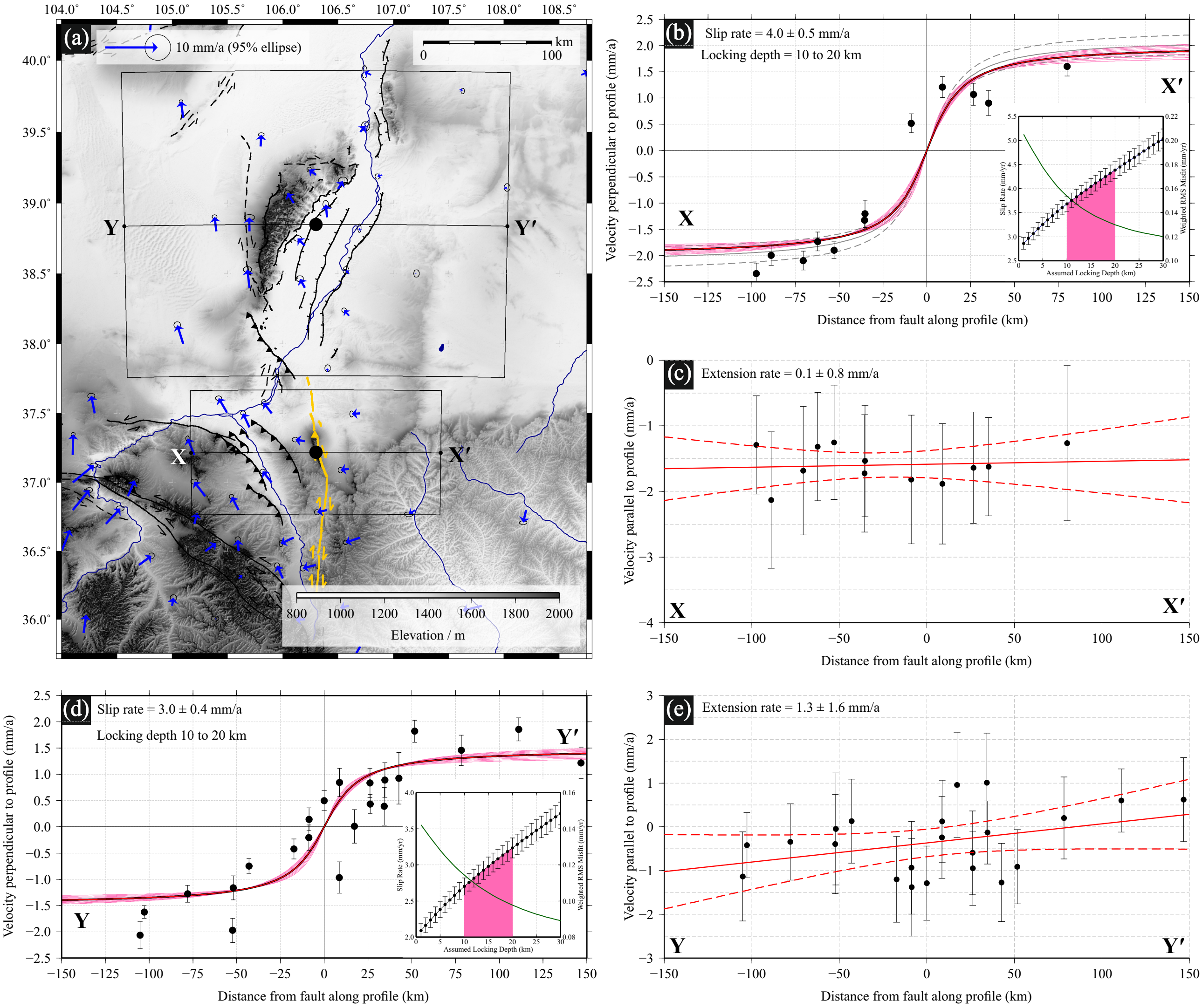
(a)
104.0° 104.5° 105.0° 105.5° 106.0° 106.5° 107.0° 107.5° 108.0° 108.5°
40.0° 39.5° 39.0° 38.5° 38.0° 37.5° 37.0° 36.5° 36.0°
10 mm/a (95% ellipse)
km
0 100
Y
Y′
X
X′
800 1000 1200 1400 1600 1800 2000
Elevation / m
(b)
Slip rate = 4.0 ± 0.5 mm/a
Locking depth = 10 to 20 km
X
X′
Velocity perpendicular to profile (mm/a)
Distance from fault along profile (km)
Slip Rate (mm/yr)
Weighted RMS Misfit (mm/yr)
Assumed Locking Depth (km)
(c)
Extension rate = 0.1 ± 0.8 mm/a
X
X′
Velocity parallel to profile (mm/a)
Distance from fault along profile (km)
(d)
Slip rate = 3.0 ± 0.4 mm/a
Locking depth 10 to 20 km
Y
Y′
Velocity perpendicular to profile (mm/a)
Distance from fault along profile (km)
Slip Rate (mm/yr)
Weighted RMS Misfit (mm/yr)
Assumed Locking Depth (km)
(e)
Extension rate = 1.3 ± 1.6 mm/a
Y
Y′
Velocity parallel to profile (mm/a)
Distance from fault along profile (km)

**Figure 16.** (a) SRTM topography (30 m resolution) of the western Ordos region, Ningxia Province, northern China [*Farr et al.*, 2007]. The Luoshan Fault and Yunwushan Fault are marked in orange. Blue vectors show campaign GPS measurements made over a period of 4 years (occupations in 2009, 2011 and 2013) [*Zhao et al.*, 2015] with a best fitting rigid body rotation (about an Euler pole at 46 °N, 72 °W, estimated from the vectors within this region) subtracted from all of the vectors. (b) Swath profile X-X′ through the GPS data showing the component of velocity perpendicular to the profile azimuth of 90 °. The red line shows the best fitting arctangent function ($u = tan^{-1}\left(\frac{x}{d}\right)$, where $u$ is the velocity, $x$ is the distance from the fault and $d$ is the locking depth). The dashed grey lines indicate the geologically determined slip rate on the Luoshan Fault of 4.3±0.4 mm/a, assuming a locking depth of 15 km. The pink lines represent the range of best fitting solutions for assumed locking depths of between 10 and 20 km. The inset figure shows the trade-off between slip rate and locking depth. For this range of locking depths, we estimate a right-lateral slip rate of 4.0±0.5 mm/a. (c) Swath profile X-X′ showing the component of velocity parallel to the profile. The red lines show the best fit least squares regression to the data and the 95% confidence envelopes on this best fit line. No shortening or extension is resolvable within error along this profile. (d) Swath profile Y-Y′ through the GPS data in the Yinchuan Graben showing the component of velocity perpendicular to the profile. Annotations as in (b). We estimate a right-lateral slip rate of 3.0±0.4 mm/a. (e) Swath profile Y-Y′ showing the component of velocity parallel to the profile. Annotations as in (c). We estimate an average extension rate across the whole profile of 1.3±1.6 mm/a.

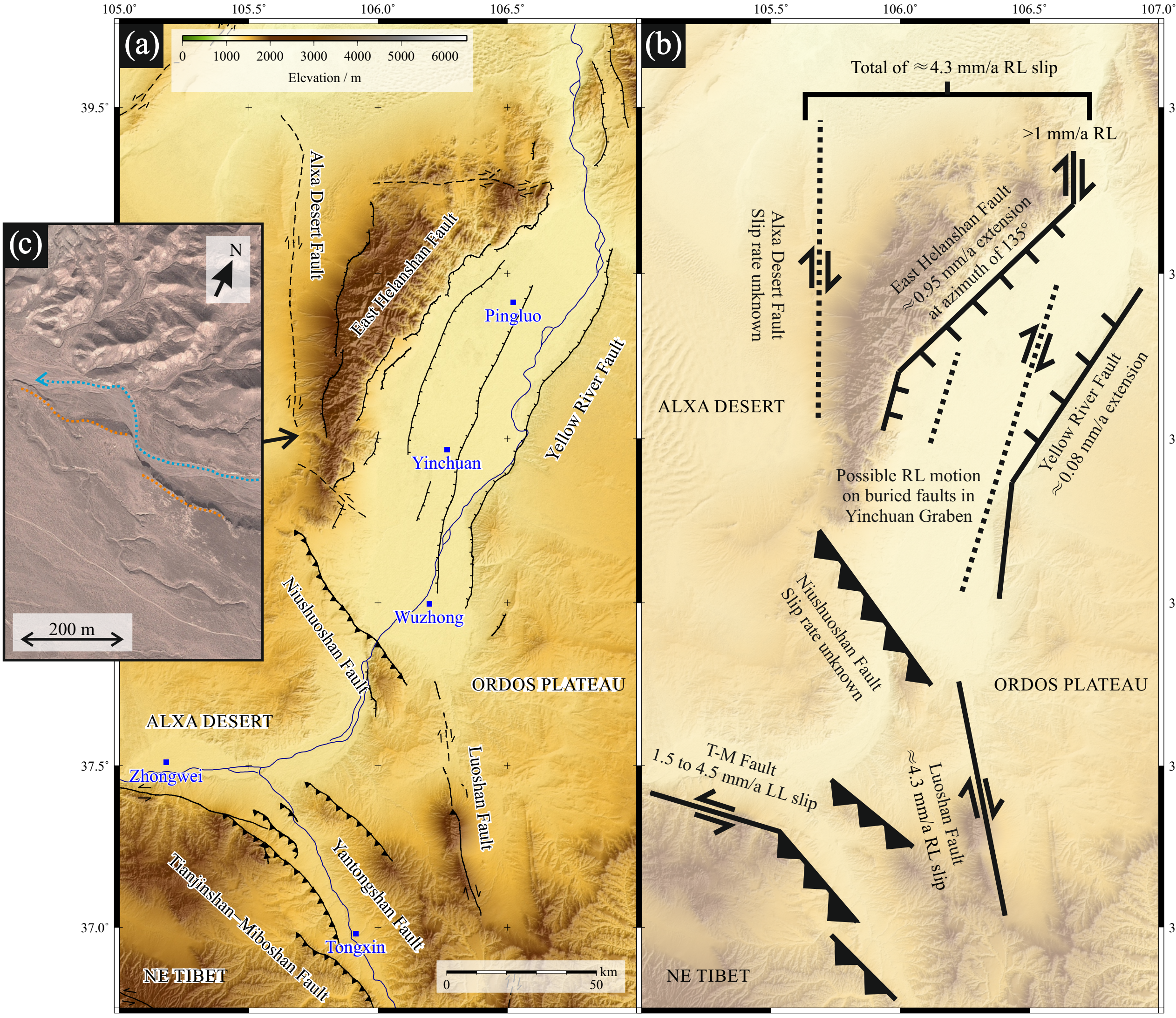
(a)
0 1000 2000 3000 4000 5000 6000
Elevation / m
105.0°
105.5°
106.0°
106.5°
39.5°
39.0°
38.5°
38.0°
37.5°
37.0°
Alxa Desert Fault
East Helanshan Fault
Pingluo
Yellow River Fault
Yinchuan
Wuzhong
Niushuoshan Fault
ORDOS PLATEAU
ALXA DESERT
Zhongwei
Luoshan Fault
Yantongshan Fault
Tianjinshan–Miboshan Fault
Tongxin
NE TIBET
km
0
50
(b)
107.0°
Total of ≈4.3 mm/a RL slip
>1 mm/a RL
Alxa Desert Fault
Slip rate unknown
East Helanshan Fault
≈0.95 mm/a extension
at azimuth of 135°
ALXA DESERT
Yellow River Fault
≈0.08 mm/a extension
Possible RL motion
on buried faults in
Yinchuan Graben
Niushuoshan Fault
Slip rate unknown
ORDOS PLATEAU
T-M Fault
1.5 to 4.5 mm/a LL slip
Luoshan Fault
≈4.3 mm/a RL slip
NE TIBET
(c)
N
200 m

**Figure 17.** (a) SRTM topography (30 m resolution) of the western Ordos region in northern China [*Farr et al.*, 2007]. Cities are marked by blue squares and faults, marked as thin black lines, have been mapped from satellite imagery (source: http://earth.google.com) based upon earlier fault maps from *Tapponnier and Molnar* [1977], *Deng et al.* [1984], *Zhang et al.* [1990], *Darby and Ritts* [2002] and *Darby et al.* [2005]. (b) Geometric model for the tectonics of the western Ordos region showing the principal faults and their slip rates, from *Zhang et al.* [1990], *Min et al.* [2003], *Deng et al.* [2004] and this study. (c) Google Earth imagery from March 2011 (source: http://earth.google.com) showing right-lateral displacement of a channel (blue) and channel riser (orange) on the Alxa Desert Fault at 38.478 °N, 105.721 °E.

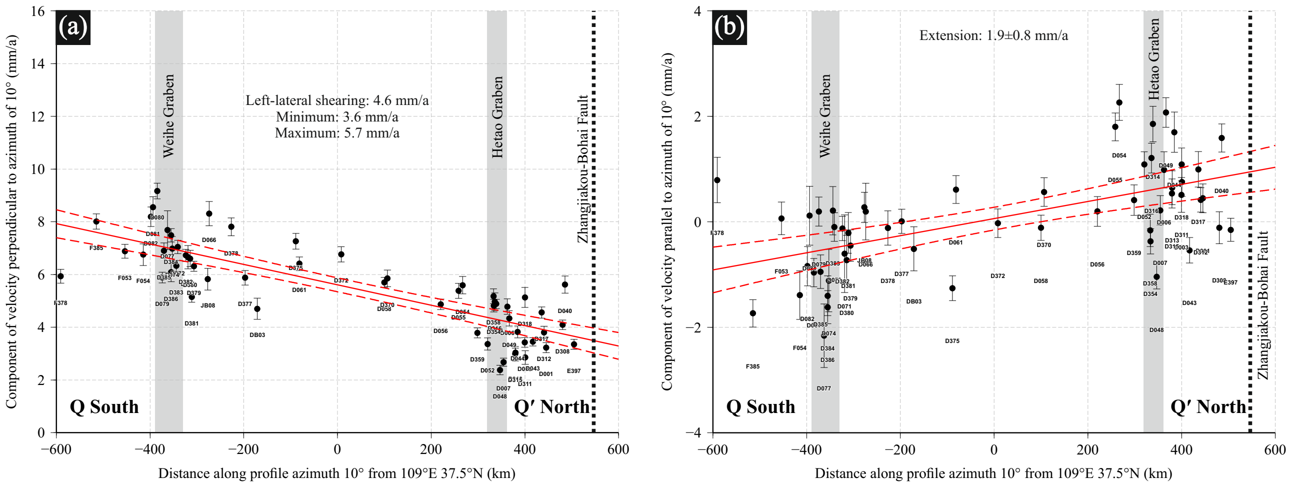

**Figure 18.** (a) Swath profile Q-Q′ through the GPS data from *Zhao et al.* [2015] showing the velocity component perpendicular to the profile azimuth of 10 °—same as Figure 2 (c). (See Figure 2 (a) for location.) The red line is the best fit least squares regression to the data and the dashed red lines are the 95% confidence envelopes on this best fit line. The profile shows left-lateral shearing of 4.6±1.1 mm/a averaged over the extent of the profile. (b) Same as (a), but showing velocities parallel to an azimuth of 10 °. The profile shows north-south extension of 1.9±0.8 mm/a averaged over the extent of the profile.

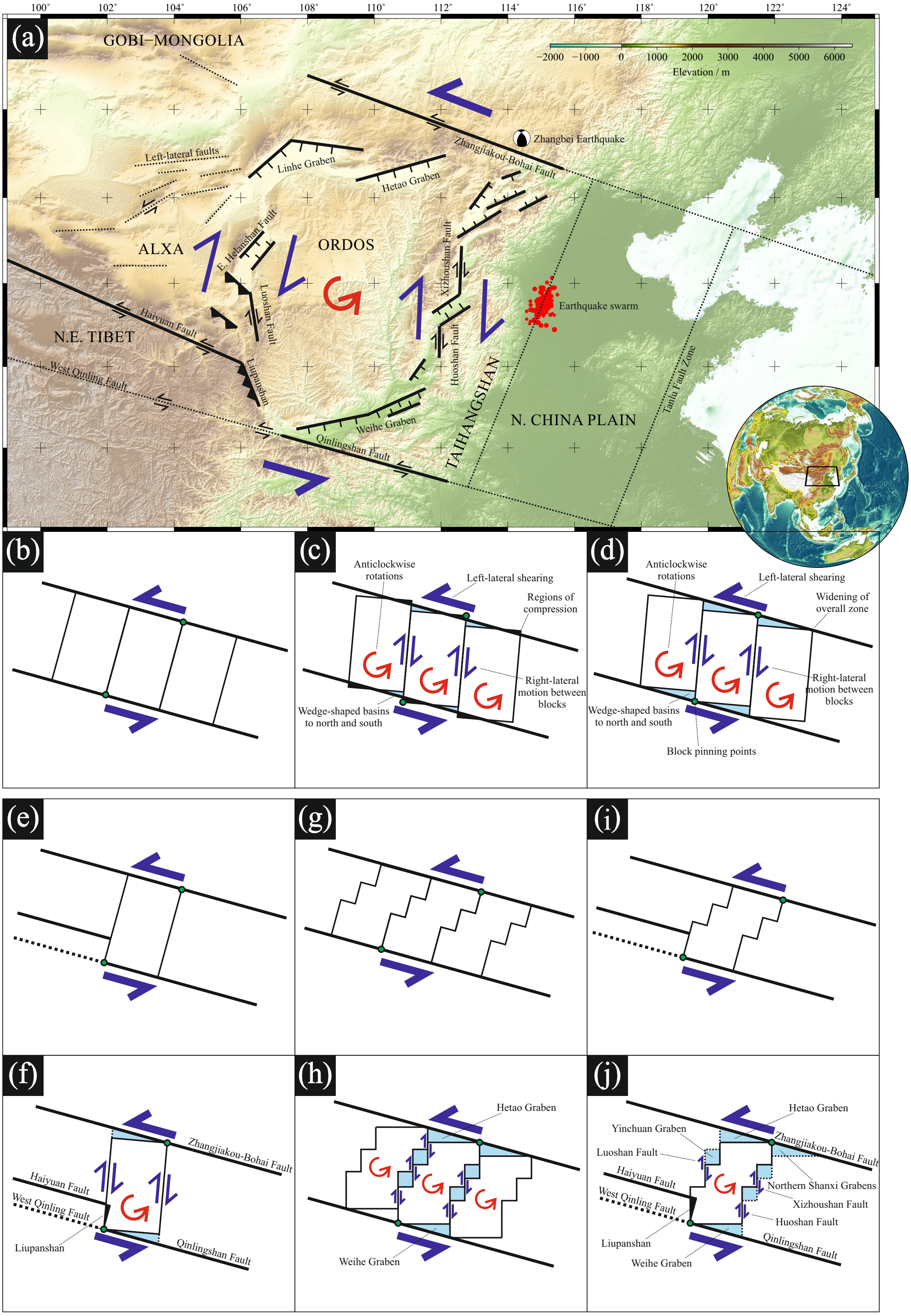
(a)
100° 102° 104° 106° 108° 110° 112° 114° 116° 118° 120° 122° 124°
44° 42° 40° 38° 36° 34°
GOBI–MONGOLIA
−2000 −1000 0 1000 2000 3000 4000 5000 6000
Elevation / m
Zhangbei Earthquake
Zhangjiakou-Bohai Fault
Left-lateral faults
Linhe Graben
Hetao Graben
ALXA
E. Helanshan Fault
ORDOS
Xizhoushan Fault
Earthquake swarm
Luoshan Fault
Huoshan Fault
Haiyuan Fault
N.E. TIBET
Liupanshan
West Qinling Fault
Weihe Graben
TAIHANGSHAN
N. CHINA PLAIN
Tanlu Fault Zone
Qinlingshan Fault
(b)
(c)
Anticlockwise rotations
Left-lateral shearing
Regions of compression
Right-lateral motion between blocks
Wedge-shaped basins to north and south
(d)
Anticlockwise rotations
Left-lateral shearing
Widening of overall zone
Right-lateral motion between blocks
Wedge-shaped basins to north and south
Block pinning points
(e)
(g)
(i)
(f)
Zhangjiakou-Bohai Fault
Haiyuan Fault
West Qinling Fault
Liupanshan
Qinlingshan Fault
(h)
Hetao Graben
Weihe Graben
(j)
Hetao Graben
Yinchuan Graben
Luoshan Fault
Zhangjiakou-Bohai Fault
Haiyuan Fault
Northern Shanxi Grabens
West Qinling Fault
Xizhoushan Fault
Huoshan Fault
Liupanshan
Qinlingshan Fault
Weihe Graben

**Figure 19.** (a) SRTM topography of the Ordos Plateau in northeastern China [*Farr et al.*, 2007]. Inset globe shows the location of Figure 19 (a) within Asia. Black lines indicate major faults or fault zones and their sense of movement. Dotted lines show possible additional blocks—the Taihangshan and North China Plain blocks—to the east of the Ordos Plateau. General kinematic scheme after *Xu and Ma* [1992], *Xu et al.* [1993] and *Xu et al.* [1994]. (b), (c) and (d) Before and (two possible) after views showing a schematic kinematic representation of the anticlockwise rotation of three crustal blocks in a WNW-ESE left-lateral shear zone. (c) and (d) indicate that for the rotation to be accommodated, either compression must occur at the NE and SW corners of each block, or the overall zone has to widen. (e) and (f) Before and after views showing a more realistic geometry for the Haiyuan Fault and the resulting development of the Liupanshan. (g) and (h) Before and after views showing how corrugated block boundaries can lead to the development of en-echelon grabens with intervening right-lateral faults (e.g. the Luoshan, Huoshan and Xizhoushan Faults). (i) and (j) Before and after views combining the above modifications into a single schematic kinematic representation.